

---

# DETECTION OF CLOUDS IN MULTIPLE WIND VELOCITY FIELDS USING GROUND-BASED INFRARED SKY IMAGES

---

**Guillermo Terrén-Serrano**

Department of Electrical and Computer Engineering  
The University of New Mexico  
Albuquerque, NM 87131, United States  
guillermoterren@unm.edu

**Manel Martínez-Ramón**

Department of Electrical and Computer Engineering  
The University of New Mexico  
Albuquerque, NM 87131, United States  
manel@unm.edu

September 3, 2022

## ABSTRACT

Horizontal atmospheric wind shear causes wind velocity fields to have different directions and speeds. In images of clouds acquired using ground-based sky imaging systems, clouds may be moving in different wind layers. To increase the performance of a global solar irradiance forecasting algorithm, it is important to detect of multiple layers of clouds. The information obtained from a global solar irradiance forecasting algorithm is necessary to optimize and schedule the solar generation resources and storage devices in a smart grid. This investigation studies the performance of unsupervised learning techniques when detecting the number of cloud layers in cloud images. The images are acquired using an innovative infrared sky imaging system mounted on a solar tracker. Different mixture models are used to infer the distribution of the cloud features. The optimal number of clusters in the mixture models is decided after implementing different Bayesian metrics and comparing these with a temporal Ising model. The motion vectors are computed using a pyramidal weighted implementation of the Lucas-Kanade algorithm. The correlations between the cloud velocity vectors and temperatures are analyzed to find the method that leads to the most accurate results. We have found that the temporal Ising model outperformed the detection accuracy of the Bayesian metrics.

**Keywords** Cloud Detection · Machine Learning · Markov Random Field · Mixture Models · Pyramidal Weighted Lucas-Kanade · Sky Imaging · Solar Forecasting

## 1 Introduction

The ongoing transition toward energy generation systems that produce low-carbon emissions is increasing the penetration of renewable energies in the power grid [1]. However, only three renewable sources can produce enough power to fulfill the demand: geothermal, biomass and solar. In particular, solar energy has the potential to become the primary source of power due to its availability and capability [2]. A Smart Grid (SG) may optimize the dispatch of energy in large Photovoltaic (PV) power plants to meet demand using recent advances in information and communication technologies [3].

The power generated by PV systems is affected by Global Solar Irradiance (GSI) fluctuations that reach the surface of PV panels [4]. Shadows projected by moving clouds produce mismatch losses [5]. Certain configurations of PV arrays reduce the impact of the losses, but they still are outside of the allowed range demanded by grid operators [6]. Forecasting of power output will equip a SG powered by PV systems with the technology necessary for regulating the dispatch of energy [7, 8]. Nevertheless, PV power plants have different physical configurations [9]. PV cells and batteries degrade following unique patterns [10]. For these reasons, the predicted power output cannot be directly extrapolated among the PV systems connected to the same SG [11, 12, 13, 14]. The forecasting of GSI over a grid projected on the Earth's surface facilitates the prediction of power output from PV systems located within the span of the grid [15, 16].

The formation of clouds is a phenomena restricted by the Tropopause [17]. Different types of clouds are expected to form at different altitudes within the Troposphere [18]. The magnitude of the wind velocity field increases with the altitude in the lower atmosphere [19, 20]. The wind gradient may also change direction due to the friction of the wind with the surface of the Earth. The planetary boundary layer (the lowest part of the Troposphere) [21] is the point where the wind shear causes low level clouds to move in a different direction and speed of that from high level clouds [22, 23, 24].

Numerical Weather Prediction (NWP) models are computationally expensive for the forecasting resolution necessary in these applications [25, 26, 27, 28, 29, 30]. GSI forecasting models which include ground weather features from meso-scale meteorology have problems of collinearity [31]. Cloud information extracted from geostationary satellite images improved the performance of solar irradiance forecasting with respect to NWP models [32, 33]. However, real-time applications of GSI forecasting using satellite imaging are not feasible due to communications delays [34, 35]. Ground-based sky imaging systems are an efficient and low-cost alternative to satellite imaging [36, 37, 38]. The performances of solar irradiance or PV power output forecasting algorithms are increased when visible and infrared (IR) ground-based sky imaging systems are installed on a solar tracker [39, 40].

Attaching a fish-eye lens to a low-cost visible light camera can provide sky images with large Field of View (FOV) [41, 42]. The disadvantage of using visible light sky imaging systems in solar forecasting is that the intensity of the pixels in the circumsolar area are saturated [43]. Radiometric long-wave IR cameras of uncooled microbolometers are low-cost and widely available [44]. These types of cameras have been used to analyze the radiation emitted by gases and clouds in the atmosphere [45]. Cloud statistics may be computed [46] to establish optical links for applications that involve Earth-space communication [47]. The measured temperature of clouds depends on the air temperature on the ground [48], so the calibration of these cameras is important to perform accurate measurements [49]. Merging thermal images acquired from multiple IR cameras mounted on a dome-shaped plane can provide thermal images with larger FOV [50].

The wind velocity field shown in a sequence of cloud images is a physical process that is assumed to have a limited complexity [51]. A sequence of IR images allow the derivation of physical features from moving clouds in a wind velocity field. These are more interpretable for modelling physical processes. The features are temperature, velocity vectors, and height [52, 53]. It has been found that the advantage of using unsupervised learning algorithms is that the response to a sequence of images is expected to depend on the physical process that the images represent rather than the intensity of their pixels [54]. Unsupervised learning methods, in special mixture models infer the probability density functions of the observations without prior information [55].

Markov Random Fields (MRFs) were first introduced as the Ising model in statistical mechanics to model the ferromagnetic properties of certain materials [56]. These models are popular in computer vision applications in which an image is modelled as a 2-dimensional lattice graph [57]. MRFs have been used to detect and analyzed temperature distributions of images acquired from IR thermal imaging systems [58]. It possible to extend the MRFs to model spatio-temporal problems as stochastic physical processes [59, 60], image classification [61] and object tracking [62].

The unsupervised learning algorithm proposed in this investigation does inference over the number of wind velocity fields in a sequence of images using features extracted from the clouds. IR images of clouds are obtained using an innovative Data Acquisition (DAQ) system mounted in a solar tracker [48]. The velocity vectors are computed using a weighted-pyramidal variation of the standard Lucas-Kanade (LK) method [63]. The velocity vector of each pixel is computed in a weighted window of neighboring pixels. The dimension of the image and the weights are reduced in proportion to scale-level of the number of pyramids applied in the implementation. The computed velocity vector in the pyramidal scale-levels are extrapolated to the the original dimensions of the image and average together. The weight of a pixel is the posterior probability of belonging to the lower or the upper cloud layer. The obtained velocity vectors for each cloud layer are averaged together weighting them by the posterior probability of each cloud layer.

A real-time probabilistic model is implemented to detect the number of layers in an IR image [64]. The proposed model is a temporal variation of a MRF that models the hidden process of the number of wind velocity fields in a sequence of images [65, 66]. The motion of clouds on a sequence of images are used to calculate the velocity vectors. The temperature and height of the pixels are also extracted from the cloud images. The distributions of the features are inferred with different parametric mixture models [67, 68]. The mixture models are optimized using the Expectation-Maximization (EM) algorithm [69, 70]. The label switching of the mixture models is solved using the average height of each distribution in the mixture model [71].

## 2 Methodology

The IR sensor provides an uniform thermal image as output. When the radiometry functionality is enabled the pixels in a frame, are turned into temperature measurements. A pixel of the camera frame is defined by a pair of euclidean coordinates  $\mathbf{X} = \{(x, y)_{i,j} \mid \forall i = 1, \dots, M, \forall j = 1, \dots, N\}$ , and the temperature of each one of the pixels is defined in Kelvin degrees as  $\mathbf{T}^{(t)} = \{T_{i,j}^{(t)} \in \mathbb{R} \mid \forall i = 1, \dots, M, \forall j = 1, \dots, N\}$ , where  $t$  represents a process defined as  $t \in (0, \infty]$ , that is a sequence of IR images ordered chronologically by capturing time. The temperature of a particle in the Troposphere is a function of the height [72]. The height of a pixel in a frame can be approximated using the Moist Adiabatic Lapse Rate (MALR) function, that we define as  $\phi : T \mapsto h$ , knowing the temperatures obtained with the IR camera. The height of each one of the pixels in a frame are  $\mathbf{H}^{(t)} = \{H_{i,j}^{(t)} \in \mathbb{R} \mid \forall i = 1, \dots, M, \forall j = 1, \dots, N\}$ .

When there are multiple layers of clouds in an image, a mixture model is expected to have multiple clusters. In order to infer the distribution of the temperatures or heights using a Beta Mixture Model (BeMM), the features are first normalized to the domain of a beta distribution  $\bar{T}_{i,j} = [T_{i,j}^{(t)} - \min(\mathbf{T}^{(t)})]/[\max(\mathbf{T}^{(t)}) - \min(\mathbf{T}^{(t)})]$ . When the inference is performed with a Gamma Mixture Model (GaMM), the temperatures are normalized to the domain of the gamma distribution  $\tilde{T}_{i,j} = T_{i,j}^{(t)} - \min(\mathbf{T}^{(t)})$ . The heights (in kilometers) are within the domain of the gamma distribution. When the inference is performed using a Gaussian Mixture Model (GMM), the temperatures and heights do not require normalization.

### 2.1 Pyramidal Weighted Lucas Kanade

In current computer vision literature, there are three primary techniques to estimate the motion of objects in a sequence of images: the Lucas-Kanade [63], Horn-Schunck [73] and Farnebäck [74]. These three methods are based on the space-time partial derivatives between two consecutive frames. The techniques to estimate the motion vectors in an image are sensitive to the intensity gradient of the pixels. An atmospheric model is implemented to remove the gradient produced by the Sun's direct irradiance and the atmospheric scattered irradiance. Both of which routinely appear on the images in the course of the year. A persistent model of the outdoor germanium window of the IR camera removes debris and water spots that appear in the image [75]. A series of sequences of images with clouds flowing different directions were simulated to cross-validate the set of parameters for each one of the mentioned methods. The Pyramidal Weighted Lucas-Kanade (PWLK) method was found to be the most suitable for this application [76].

#### 2.1.1 Optical Flow

The optical flow equation considers that exists a small displacement  $\Delta x$  and  $\Delta y$  in the direction of an object in an image. The object is assumed to have constant intensity  $\mathcal{I}$  between two consecutive frames. The frames are separated in time by small time increment  $\Delta t$ ,

$$\mathcal{I}(x, y, t) = \mathcal{I}(x + \Delta x, y + \Delta y, t + \Delta t). \quad (1)$$

Assuming that the difference in intensity between neighboring pixels is smooth and that brightness of a pixel in consecutive frames is constant, the Taylor series expansion is applied and following equation obtained,

$$\mathcal{I}(x + \Delta x, y + \Delta y, t + \Delta t) = \mathcal{I}(x, y, t) + \frac{\partial \mathcal{I}}{\partial x} \Delta x + \frac{\partial \mathcal{I}}{\partial y} \Delta y + \frac{\partial \mathcal{I}}{\partial t} \Delta t. \quad (2)$$

The factors are simplified combining the last two equation,

$$\frac{\partial \mathcal{I}}{\partial x} \Delta x + \frac{\partial \mathcal{I}}{\partial y} \Delta y + \frac{\partial \mathcal{I}}{\partial t} \Delta t = 0. \quad (3)$$

The velocity of an object is derived dividing the terms of the displacement by the increment of time  $\Delta t$ ,

$$\frac{\partial \mathcal{I}}{\partial x} \frac{\Delta x}{\Delta t} + \frac{\partial \mathcal{I}}{\partial y} \frac{\Delta y}{\Delta t} + \frac{\partial \mathcal{I}}{\partial t} \frac{\Delta t}{\Delta t} = 0. \quad (4)$$

The velocity components are defined as  $v_x$  and  $v_y$  so that,

$$\frac{\partial \mathcal{I}}{\partial x} v_x + \frac{\partial \mathcal{I}}{\partial y} v_y + \frac{\partial \mathcal{I}}{\partial t} = 0. \quad (5)$$

This equation is known as the aperture problem,

$$\mathcal{I}_x v_x + \mathcal{I}_y v_y = -\mathcal{I}_t, \quad (6)$$

where  $\mathcal{I}_x = \partial \mathcal{I} / \partial x$ ,  $\mathcal{I}_y = \partial \mathcal{I} / \partial y$  and  $\mathcal{I}_t = \partial \mathcal{I} / \partial t$  are the derivatives for notation simplification.

The 2-dimensional derivatives are approximated using convolutional filters in a image [77]. The intensity of pixels a frame in time instant  $t$  are  $\mathbf{I}^{(t)} = \{i_{i,j}^{(t)} \in \mathbb{R}^{[0,2^8]} \mid i = 1, \dots, N, j = 1, \dots, M\}$ . The Sobel method to compute the derivatives is implemented [78],

$$\begin{aligned}\mathbf{I}'_x &= \mathbf{I}^{(t-1)} \star \mathbf{K}_x \\ \mathbf{I}'_y &= \mathbf{I}^{(t-1)} \star \mathbf{K}_y \\ \mathbf{I}'_t &= \mathbf{I}^{(t-1)} \star (\mathbf{K}_t \sigma) + \mathbf{I}^{(t)} \star (-\mathbf{K}_{(t)} \sigma)\end{aligned}\quad (7)$$

where  $\star$  represent a 2-dimensional convolution.  $\mathbf{K}_x$ ,  $\mathbf{K}_y$  and  $\mathbf{K}_t$  are the derivative kernels in the x, y and t direction respectively.  $\mathbf{I}^{(t-1)}$  and  $\mathbf{I}^{(t)}$  are the first and second consecutive frames. The parameter  $\sigma$  is amplitude of the temporal differential kernel. This parameter may be cross-validated when the velocity field is known.

### 2.1.2 Lucas-Kanade

The LK method proposes to find the solution for the optical flow equations via Least-Squares (LS). In this research, the LK method is extended to multiple pyramidal levels. The Euclidean coordinate pairs of pixel in an image, are defined as  $\mathbf{X}_k = \{(x, y)_{i,j,k} \in \mathbb{N} \mid i = 1, \dots, N/k, j = 1, \dots, M/k\}$ , for each pyramidal level  $k$ . The neighborhood of pixels within the sliding windows is,

$$\mathbf{x} = \{\mathbf{x}_{i+n,j+m} \in \mathbb{N}^2 \mid n = -w, \dots, +w, m = -w, \dots, +w, \} \in \mathbb{N}^W, \quad (8)$$

where  $i, j$  is the pixel where the sliding windows is centered, and  $W = 2w + 1$  is the size of the windows. The parameter  $w \in \mathbb{N}$  has to be cross-validated.

The pixels' differentials in each pyramidal level are interpolated using bilinear method [79]. The interpolating functions are defined independently as  $\mathcal{I}_x : \mathbf{x} \mapsto x_1 \in \mathbb{R}$ ,  $\mathcal{I}_y : \mathbf{x} \mapsto x_2 \in \mathbb{R}$ ,  $\mathcal{I}_t : \mathbf{x} \mapsto y \in \mathbb{R}$ . The set of independent and depended variables used to find the WLS solution in matrix form is,

$$\mathbf{X}_{i,j,k} = \begin{bmatrix} \mathcal{I}_x(\mathbf{x}_1) & \mathcal{I}_y(\mathbf{x}_1) \\ \mathcal{I}_x(\mathbf{x}_2) & \mathcal{I}_y(\mathbf{x}_2) \\ \vdots & \vdots \\ \mathcal{I}_x(\mathbf{x}_W) & \mathcal{I}_y(\mathbf{x}_W) \end{bmatrix}; \quad \mathbf{w}_{i,j,k} = \begin{bmatrix} v_x \\ v_y \end{bmatrix}; \quad \mathbf{y}_{i,j,k} = \begin{bmatrix} -\mathcal{I}_t(\mathbf{x}_1) \\ -\mathcal{I}_t(\mathbf{x}_2) \\ \vdots \\ -\mathcal{I}_t(\mathbf{x}_W) \end{bmatrix} \quad (9)$$

Instead of the ordinal weighting of the neighboring pixels in the window using the probabilities of normal distribution, the solution of the LK is extended to a Weighted Least-Squares (WLS) [76], which weights are the posterior probabilities of a given wind velocity field in a pixel. The scaling matrix of probabilities is  $\mathbf{\Gamma}_{i,j,k} = \mathbf{I}_{N_k \times N_k} \cdot \boldsymbol{\gamma}_k^\top$ , which matrix form is,

$$\mathbf{\Gamma}_{i,j,k} = \begin{bmatrix} \gamma_1 & 0 & \dots & 0 \\ 0 & \gamma_2 & \ddots & \vdots \\ \vdots & \ddots & \ddots & 0 \\ 0 & \dots & 0 & \gamma_{N_k} \end{bmatrix} \quad (10)$$

The analytical solution of the WLK problem for each coordinate  $i, j$  in each pyramid level  $k$  is,

$$\begin{aligned}\mathbf{X}_{i,j,k}^\top \mathbf{\Gamma}_{i,j,k} \mathbf{X}_{i,j,k} \mathbf{w}_{i,j,k} &= \mathbf{X}_{i,j,k}^\top \mathbf{\Gamma}_{i,j,k} \mathbf{y}_{i,j,k} \\ \mathbf{w}_{i,j,k} &= (\mathbf{X}^\top \mathbf{\Gamma}_{i,j,k} \mathbf{X}_{i,j,k})^{-1} \mathbf{X}_{i,j,k}^\top \mathbf{\Gamma}_{i,j,k} \mathbf{y}_{i,j,k},\end{aligned}\quad (11)$$

and this might be an ill-conditioned problem. The eigenvalues of the covariance matrix are,

$$\mathbf{X}_{i,j,k}^\top \mathbf{\Gamma}_{i,j,k} \mathbf{X}_{i,j,k} = \mathbf{1} \begin{bmatrix} \lambda_1 & 0 \\ 0 & \lambda_2 \end{bmatrix} \mathbf{1}, \quad (12)$$

where  $\mathbf{1}$  is an unitary matrix of size  $2 \times 2$ ,  $\lambda_1$  and  $\lambda_2$  has to be non-zero. Therefore, to apply a threshold to the eigenvalues of velocities  $\mathbf{X}_{i,j,k}^\top \mathbf{\Gamma}_{i,j,k} \mathbf{X}_{i,j,k}$  such as  $\lambda_1 \geq \lambda_2 > \tau$  is equivalent to reduce the noise in the estimation. The parameter  $\tau$  has to be cross-validated.

The estimated velocity components are defined for each Euclidean coordinate pairs in each pyramid level  $k$  as  $\hat{\mathbf{V}}_{x,k} = \{v_{x,i,j,k} \in \mathbb{R} \mid i = 1, \dots, N/k, j = 1, \dots, M/k\} \in \mathbb{R}^{N/k \times M/k}$  and  $\hat{\mathbf{V}}_{y,k} = \{v_{y,i,j,k} \in \mathbb{R} \mid i =$

$1, \dots, N/k, j = 1, \dots, M/k \} \in \mathbb{R}^{N/k \times M/k}$ . The velocity field is extrapolated to the original Euclidean frame of reference. Bi-linear interpolation method is implemented to estimate the functions. The functions are defined as  $\mathcal{V}_x : \mathbf{x} \mapsto v_x \in \mathbb{R}$ , and  $\mathcal{V}_y : \mathbf{x} \mapsto v_y \in \mathbb{R}$ . After the application of the interpolation, the estimated velocity components are  $\hat{\mathbf{V}}_{x,k} \in \mathbb{R}^{N \times M}$  and  $\hat{\mathbf{V}}_{y,k} \in \mathbb{R}^{N \times M}$  for each pyramid level. The velocity field in an image is computed averaging the velocity fields that were estimated in each one of the pyramids,

$$\hat{\mathbf{V}}_x = \frac{\sum_{k=1}^K \hat{\mathbf{V}}_{x,k}}{K}; \quad \hat{\mathbf{V}}_y = \frac{\sum_{k=1}^K \hat{\mathbf{V}}_{y,k}}{K}, \quad (13)$$

so the result is velocity component for each pair of Euclidean coordinates in the original frame  $\mathbf{X} \in \mathbb{R}^{N \times M}$ . The velocity vectors defined in polar coordinates are  $\hat{\mathbf{R}} = (\hat{\mathbf{V}}_x + \hat{\mathbf{V}}_y)^{1/2}$ , and  $\hat{\Phi} = \text{arctan2}(\hat{\mathbf{V}}_x, \hat{\mathbf{V}}_y)$ . The optimal window size, weighted least-squares regularization, differential kernel amplitude, and number of pyramids are:  $\mathcal{W} = 16$  [pixels<sup>2</sup>],  $\tau = 1 \times 10^{-8}$ ,  $\sigma = 1$  and  $\Delta = 3$  respectively. The scale of the pyramids is set to  $\delta = 1/2$  in all levels.

The mixture model used to infer the distribution of the velocity vectors is expected to have multiple clusters when there are multiple wind velocity fields in the image. The distribution of the velocity vectors defined in Cartesian coordinates is inferred with a multivariate GMM. The inference of the velocity vectors when are defined in polar coordinates, is performed independently for each component using a GaMM and Von Mises Mixture Model (VMMM) for the magnitude and the angle respectively.

## 2.2 Maximum a Posterior Mixture Model

When the clouds are moving in multiple wind velocity fields the distributions of the temperatures, heights and velocity vectors components are expected to have multiple clusters. Mixture models are implemented to infer the distributions of the physical features extracted from IR cloud images. These physical features have different domain so the inference is implemented using probability functions which have the same domain. The objective is to find the probability function that approximates better the actual distribution of a features with the aim of detecting the most likely number of wind velocity fields on an image. The formulation of the proposed mixture models includes a prior distribution on the cluster weights to avoid over-fitting.

### 2.2.1 Expectation-Maximization

The optimal set of parameters in a mixture model can be computed using the EM algorithm. The implementation of the EM algorithm guarantees a smooth convergence to a local maxima following an iterative approach consisting of two steps [69]. The maximized function is the expected complete data log-likelihood,

$$\begin{aligned} \mathcal{Q}(\boldsymbol{\theta}^{(t)}, \boldsymbol{\theta}^{(t-1)}) &\triangleq \mathbb{E} \left[ \sum_{i=1}^N \log p(x_i, z_i | \boldsymbol{\theta}^{(t)}) + \log p(\boldsymbol{\pi} | \boldsymbol{\alpha}) \right] \\ &= \sum_{i=1}^N \mathbb{E} \left[ \log \left( \prod_{k=1}^K \left[ \pi_k p(x_i | \boldsymbol{\theta}_k^{(t)}) \right]^{\mathbb{I}(z_i=k)} \right) \right] + \log p(\boldsymbol{\pi} | \boldsymbol{\alpha}) \\ &= \sum_{i=1}^N \sum_{k=1}^K p(z_i = k | x_i, \boldsymbol{\theta}_k^{(t-1)}) \log \left[ \pi_k p(x_i | \boldsymbol{\theta}_k^{(t)}) \right] + \log p(\boldsymbol{\pi} | \boldsymbol{\alpha}), \end{aligned} \quad (14)$$

where  $\mathbb{I}(\cdot)$  is the indicator function and  $t$  represents the last iteration.

The initialization of the EM starts by randomly assigning a set of parameters and a prior. In the expectation step of the EM algorithm, a posterior  $\gamma_{i,k}$  is assigned to each sample using the likelihood function,

$$\gamma_{i,k} = \frac{\pi_k p(x_i | \boldsymbol{\theta}_k^{(t-1)})}{\sum_{k=1}^K \pi_k p(x_i | \boldsymbol{\theta}_k^{(t-1)})}. \quad (15)$$

In the maximization step, the parameters that maximize the complete data log-likelihood plus the log-prior are found,

$$\mathcal{Q}(\boldsymbol{\theta}^{(t)}, \boldsymbol{\theta}^{(t-1)}) = \sum_{i=1}^N \sum_{k=1}^K \gamma_{i,k} \log \pi_k + \sum_{i=1}^N \sum_{k=1}^K \gamma_{i,k} \log p(x_i | \boldsymbol{\theta}_k^{(t)}) + \log p(\boldsymbol{\pi} | \boldsymbol{\alpha}) \quad (16)$$

where  $\gamma_{i,k} \triangleq p(z_i = k \mid x_i, \boldsymbol{\theta}^{(t-1)}, \boldsymbol{\alpha})$  is the responsibility of the cluster  $k$  in the sample  $i$ . The prior  $p(\boldsymbol{\pi} \mid \boldsymbol{\alpha})$  is a Dirichlet distribution  $\boldsymbol{\pi} \sim \text{Dir}(\boldsymbol{\alpha})$ , and  $\alpha_k \geq 1$ . The mixture weights are updated using the posterior probabilities,

$$\pi_k = \frac{\alpha_k - 1 + \sum_{i=1}^N \gamma_{i,k}}{N - K + \sum_{k=1}^K \alpha_k}. \quad (17)$$

when  $\alpha_k = 1$ , the prior is noninformative  $p(\boldsymbol{\pi} \mid \boldsymbol{\alpha}) = 0$  and thus the MAP estimation is equivalent to the ML [70],  $\pi_k = [\sum_{i=1}^N \gamma_{i,k}]/N$ .

The E and M steps are repeated until the complete data log-likelihood have converged to a local maxima. In the case of a quadratic loss function this problem has analytical solution, for instance in a GMM [70]. When the loss function has not analytical solution, it can be solved implementing a numerical optimization method based on the gradient.

### 2.2.2 Gamma Mixture Model

The distribution of the magnitude of velocity vectors or the heights can be approximate by mixture of gamma distributions  $X \sim \mathcal{G}(\alpha, \beta)$  which density function is,

$$f(x; \alpha, \beta) = \frac{x^{\alpha-1} e^{-\frac{x}{\beta}}}{\beta^\alpha \Gamma(\alpha)} \quad x > 0, \quad \alpha, \beta > 0, \quad (18)$$

the gamma function is  $\Gamma(\alpha) = (\alpha - 1)!$ .

The log-likelihood of the gamma density function needed to compute the expected complete data log-likelihood in a GaMM is,

$$\log p(x_i \mid \alpha_k, \beta_k) = (\alpha_k - 1) \log x_i - \frac{x_i}{\beta_k} - \alpha_k \log \beta_k - \log \Gamma(\alpha_k). \quad (19)$$

The maximization step has to be solved via numerical optimization. The gradient w.r.t.  $\alpha_k$  is,

$$\begin{aligned} \frac{\partial \mathcal{L}(\boldsymbol{\theta}_k)}{\partial \alpha_k} &= \sum_{k=1}^K \sum_{i=1}^N \gamma_{i,k} \frac{\partial}{\partial \alpha_k} \log p(x_i \mid \alpha_k, \beta_k) \\ &= \sum_{k=1}^K \sum_{i=1}^N \gamma_{i,k} \left[ \log x_i - \log \beta_k - \frac{\Gamma'(\alpha_k)}{\Gamma(\alpha_k)} \right], \end{aligned} \quad (20)$$

where  $\Gamma'(\alpha) = -\Gamma(\alpha)[\frac{1}{\alpha} + \gamma + \sum_{n=1}^{\infty} (\frac{1}{n+\alpha} - \frac{1}{n})]$ , and  $\gamma$  is the Euler-Mascheroni constant. The gradient w.r.t.  $\beta_k$  is,

$$\begin{aligned} \frac{\partial \mathcal{L}(\boldsymbol{\theta}_k)}{\partial \beta_k} &= \sum_{k=1}^K \sum_{i=1}^N \gamma_{i,k} \left[ \frac{\partial}{\partial \beta_k} \log p(x_i \mid \alpha_k, \beta_k) \right] \\ &= \sum_{k=1}^K \sum_{i=1}^N \gamma_{i,k} \left[ \frac{1}{\beta_k} \left( \frac{x_i}{\beta_k} - \alpha_k \right) \right]. \end{aligned} \quad (21)$$

The generalization of the gamma distribution for multiple dimension do not have an unified expression. In fact, the multivariate gamma distribution is unknown in the exponential family [80].

### 2.2.3 Bivariate Gamma Mixture Model

The distribution of magnitude of velocity vectors and heights can be approximated by mixture of bivariate gamma distributions  $X, Y \sim \mathcal{BG}(\alpha, \beta, a)$  which density function is [80],

$$f(x, y; \alpha, \beta, a) = \frac{\beta^\alpha x^{\alpha+\alpha-1} y^{\alpha-1}}{\Gamma(a) \Gamma(\alpha)} e^{-\beta x} e^{-\beta y} \quad x, y > 0, \quad (22)$$

where the gamma function is  $\Gamma(\alpha) = (\alpha - 1)!$ , and the parameters are  $\alpha, \beta, a > 0$ .

The log-likelihood of the bivariate gamma density function needed for computing the expected complete data log-likelihood in a Bivariate Gamma Mixture Model (BGaMM) is,

$$\begin{aligned} \log p(x_i, y_i \mid \alpha_k, \beta_k, a_k) &= \alpha_k \log \beta_k + (\alpha_k + a_k - 1) \log x_i + \dots \\ &\dots + (a_k - 1) \log y_i - \beta_k x_i - x_i y_i - \log \Gamma(\alpha_k) - \log \Gamma(a_k) \end{aligned} \quad (23)$$

As the loss function has not analytical solution, the maximization step is solved by numerical optimization. The gradient w.r.t.  $\alpha_k$  is,

$$\begin{aligned}\frac{\partial \mathcal{L}(\boldsymbol{\theta}_k)}{\partial \alpha_k} &= \sum_{k=1}^K \sum_{i=1}^N \gamma_{i,k} \frac{\partial}{\partial \alpha_k} \log p(x_i, y_i | \alpha_k, \beta_k, a_k) \\ &= \sum_{k=1}^K \sum_{i=1}^N \gamma_{i,k} \left[ \log \beta_k + \log x_i - \frac{\Gamma'(\alpha_k)}{\Gamma(\alpha_k)} \right].\end{aligned}\quad (24)$$

The gradient w.r.t.  $\beta_k$  is,

$$\begin{aligned}\frac{\partial \mathcal{L}(\boldsymbol{\theta}_k)}{\partial \beta_k} &= \sum_{k=1}^K \sum_{i=1}^N \gamma_{i,k} \left[ \frac{\partial}{\partial \beta_k} \log p(x_i | \alpha_k, \beta_k, a_k) \right] \\ &= \sum_{k=1}^K \sum_{i=1}^N \gamma_{i,k} \left[ \frac{\alpha_k}{\beta_k} - x_i \right].\end{aligned}\quad (25)$$

The gradient w.r.t.  $a_k$  is,

$$\begin{aligned}\frac{\partial \mathcal{L}(\boldsymbol{\theta}_k)}{\partial a_k} &= \sum_{k=1}^K \sum_{i=1}^N \gamma_{i,k} \left[ \frac{\partial}{\partial a_k} \log p(x_i, y_i | \alpha_k, \beta_k, a_k) \right] \\ &= \sum_{k=1}^K \sum_{i=1}^N \gamma_{i,k} \left[ \log x_i + \log y_i - \frac{\Gamma'(\alpha_k)}{\Gamma(\alpha_k)} \right].\end{aligned}\quad (26)$$

Applying the independence assumption to each component of the gamma model, the general form of joint density for a multivariate gamma distribution can be derived, but it needs to be considered that exists a marginal density function for each one of random variables [80].

#### 2.2.4 Von Mises Mixture Model

The angular component of the velocity vectors is approximated by a Von Mises distribution  $X \sim \mathcal{VM}(\mu, \kappa)$ . The density function of this distribution is,

$$f(x; \mu, \kappa) = \frac{e^{\kappa \cos(x-\mu)}}{2\pi I_0(\kappa)}, \quad x, \mu \in [-\pi, \pi], \quad \kappa > 0, \quad (27)$$

where  $I_0$  represents the modified Bessel function of order 0 that has this formula,

$$I_\nu(\kappa) = \left(\frac{\kappa}{2}\right)^\nu \sum_{k=0}^{\infty} \frac{\left(\frac{1}{4}\kappa^2\right)^k}{k! \Gamma(\nu + k + 1)}. \quad (28)$$

In the case of mixture of a Von Mises distribution, the data log-likelihood for each cluster is,

$$\log p(x_i | \mu_k, \kappa_k) = \kappa_k \cos(x_i - \mu_k) - \log 2\pi - \log I_0(\kappa_k). \quad (29)$$

As mixture model without quadratic loss has not analytical solution, the maximization step is solved computing the gradient w.r.t.  $\mu_k$ ,

$$\begin{aligned}\frac{\partial \mathcal{L}(\boldsymbol{\theta}_k)}{\partial \mu_k} &= \sum_{k=1}^K \sum_{i=1}^N \gamma_{i,k} \left[ \frac{\partial}{\partial \mu_k} \log p(x_i | \mu_k, \kappa_k) \right] \\ &= \sum_{k=1}^K \sum_{i=1}^N \gamma_{i,k} [\kappa_k \sin(x_i - \mu_k)],\end{aligned}\quad (30)$$

and the gradient w.r.t.  $\kappa_k$ ,

$$\begin{aligned}\frac{\partial \mathcal{L}(\boldsymbol{\theta}_k)}{\partial \kappa_k} &= \sum_{k=1}^K \sum_{i=1}^N \gamma_{i,k} \left[ \frac{\partial}{\partial \kappa_k} \log p(x_i | \mu_k, \kappa_k) \right] \\ &= \sum_{k=1}^K \sum_{i=1}^N \gamma_{i,k} \left[ \cos(x_i - \mu_k) - \frac{I_1(\kappa_k)}{I_0(\kappa_k)} \right]\end{aligned}\quad (31)$$

where the Bessel function of order 1 is obtained from  $\partial I_0(\kappa)/\partial\kappa = I_1(\kappa)$ .

An extension for the multivariate Von Mises distribution can be found in [81], other solutions to the VMMM problem are [82, 83].

### 2.2.5 Beta Mixture Model

The distribution of the normalized temperatures or heights can be approximated by mixture of beta distributions  $X \sim \mathcal{B}(\alpha_k, \beta_k)$  which density function is,

$$f(x_i; \alpha_k, \beta_k) = \frac{1}{B(\alpha_k, \beta_k)} x_i^{\alpha_k-1} (1-x_i)^{\beta_k-1}, \quad \alpha_k, \beta_k > 0, \quad (32)$$

where  $x_i \in (0, 1)$ , beta function is  $B(\alpha_k, \beta_k) = [\Gamma(\alpha_k)\Gamma(\beta_k)]/[\Gamma(\alpha_k + \beta_k)]$ , and the gamma function is  $\Gamma(\alpha_k) = (\alpha_k - 1)!$ .

The log-likelihood of the beta density function, that is needed to compute the expected complete data log-likelihood in the mixture model is,

$$\log p(x_i | \alpha_k, \beta_k) = (\alpha_k - 1) \log x_i + (\beta_k - 1) \log(1 - x_i) - \log B(\alpha_k, \beta_k). \quad (33)$$

The maximization step has to be solved by gradient. The gradient w.r.t.  $\alpha_k$  is,

$$\begin{aligned} \frac{\partial \mathcal{L}(\theta_k)}{\partial \alpha_k} &= \sum_{k=1}^K \sum_{i=1}^N \gamma_{i,k} \frac{\partial}{\partial \alpha_k} \log p(x_i | \alpha_k, \beta_k) \\ &= \sum_{i=1}^N \gamma_{i,k} \sum_{k=1}^K [\log x_i - \psi(\alpha_k) + \psi(\alpha_k + \beta_k)], \end{aligned} \quad (34)$$

where  $\partial B(\alpha_k, \beta_k)/\partial \alpha_k = B(\alpha_k, \beta_k)[\psi(\alpha_k) - \psi(\alpha_k + \beta_k)]$ , and  $\psi(\cdot)$  is the digamma function, which is  $\psi(\alpha_k) = \Gamma'(\alpha_k)/\Gamma(\alpha_k)$ . The gradient w.r.t.  $\beta_k$  is,

$$\begin{aligned} \frac{\partial \mathcal{L}(\theta_k)}{\partial \beta_k} &= \sum_{k=1}^K \sum_{i=1}^N \gamma_{i,k} \left[ \frac{\partial}{\partial \beta_k} \log p(x_i | \alpha_k, \beta_k) \right] \\ &= \sum_{k=1}^K \sum_{i=1}^N \gamma_{i,k} [\log(-x_i) - \psi(\beta_k) + \psi(\alpha_k + \beta_k)]. \end{aligned} \quad (35)$$

In previous work carried out in the implementation of a BeMM clustering, was found that is not optimal to assign the number of clusters in these models applying BIC [84]. The authors proposed to implement ICL-BIC instead.

### 2.2.6 Gaussian Mixture Model

The distribution of the velocity components in a Cartesian coordinates system can be approximate by a mixture of multivariate normal distributions  $X \sim \mathcal{N}(\mu, \Sigma)$ . The multivariate normal likelihood is,

$$f(\mathbf{x}; \mu_k, \Sigma_k) = \frac{1}{\sqrt{(2\pi)^d |\Sigma_k|}} \cdot \exp \left\{ -\frac{1}{2} (\mathbf{x} - \mu_k)^\top \Sigma_k^{-1} (\mathbf{x} - \mu_k) \right\}, \quad (36)$$

The log-likelihood of the multivariate density function [70] for computing the expected complete data log-likelihood in the GMM is,

$$\log p(\mathbf{x}_i | \mu_k, \Sigma_k) = -\frac{d}{2} \log 2\pi - \frac{1}{2} \log |\Sigma_k| - \frac{1}{2} (\mathbf{x}_i - \mu_k)^\top \Sigma_k^{-1} (\mathbf{x}_i - \mu_k). \quad (37)$$

In the maximization stage, the mean and variance of each cluster that maximize the log-likelihood have an analytical solution that is,

$$\begin{aligned} \mu_k &= \frac{\sum_{i=1}^N \gamma_{i,k} \mathbf{x}_i}{\gamma_k} \\ \Sigma_k &= \frac{\sum_{i=1}^N \gamma_{i,k} \mathbf{x}_i \mathbf{x}_i^\top}{\gamma_k} - \mu_k \mu_k^\top. \end{aligned} \quad (38)$$

The temperatures or heights can be approximated with univariate normal distribution. The extension of the GMM is the same for the case of one variable or multiple variables. The theory behind mixture models, as well as the EM algorithm, is fully developed in [70].

### 2.3 Bayesian Metrics

The Bayesian Information Criterion (BIC) is a metric to choose between models but penalizing the models that have higher number of parameters, and have more samples [85]. The BIC in a mixture model is,

$$\begin{aligned} \mathcal{BIC}(\boldsymbol{\theta})_K &= \lambda \log N - 2 \log \mathcal{L}(\boldsymbol{\theta}) \\ &= \lambda \log N - 2 \left[ \sum_{k=1}^K \sum_{i=1}^N \gamma_{i,k} \log p(x_i | \boldsymbol{\theta}_k) \right], \end{aligned} \quad (39)$$

where  $\lambda$  is the number of parameters in the model, and  $N$  is the number of samples. As pixel is assumed to be in one wind layer or another  $\gamma_{i,k} = \{0, 1\}$ , the posterior is defined  $\gamma_{i,k} \triangleq \mathbb{I}(z_i = k)$ .

The BIC is close related to Akaike Information Criterion (AIC) [86],

$$\mathcal{AIC}(\boldsymbol{\theta})_K = 2\lambda - 2 \log \mathcal{L}(\boldsymbol{\theta}). \quad (40)$$

In other metrics, such as the Classification Likelihood Criterion (CLC),

$$\mathcal{CLC}(\boldsymbol{\theta})_K = 2\mathcal{H}(\boldsymbol{\theta}) - 2 \log \mathcal{L}(\boldsymbol{\theta}), \quad (41)$$

uses the entropy function  $\mathcal{H}(\cdot)$  in the context of information theory. CLC is similar to the AIC [87], but applying the entropy as a penalizing factor instead of the number of parameters. The entropy in a mixture model is,

$$\mathcal{H}(\boldsymbol{\theta})_K = \sum_{k=1}^K \sum_{i=1}^N \gamma_{i,k} \log \gamma_{i,k}. \quad (42)$$

The Integrated Classification Likelihood (ICL), which is

$$\mathcal{ICL}(\boldsymbol{\theta})_K = \mathcal{BIC}(\boldsymbol{\theta})_K + 2\mathcal{H}(\boldsymbol{\theta}), \quad (43)$$

is based on both BIC and the entropy.

The number of clusters  $K$  and the likelihood function, is different in each model  $\mathcal{M}_K$ , thus each model is expected to have a different  $\mathcal{BIC}(\boldsymbol{\theta})_K$ ,  $\mathcal{AIC}(\boldsymbol{\theta})_K$ ,  $\mathcal{CLC}(\boldsymbol{\theta})_K$ , and  $\mathcal{ICL}(\boldsymbol{\theta})_K$ . For all those metrics, the optimal number of clusters is when the value of the metric is the lowest.

### 2.4 Temporal Markov Random Field

The energy function of a MRF is composed of two functions [88]. The function  $\varphi$  that is the joint distribution of a class, and the function  $\psi$  that is the potential energy of the system's configuration (a term from statistical mechanics),

$$\mathcal{U}\left(y^{(t)}, \mathbf{x}_i^{(t)}\right) = \varphi\left(\mathbf{x}_i^{(t)}, y^{(t)}\right) + \psi\left(y^{(t)}, y^{(t-1)}\right), \quad (44)$$

where  $\mathbf{x}_i^{(t)}$  are the features of sample  $i$  and  $y^{(t)}$  is number of wind velocity fields in frame  $t$ .

A probabilistic perspective is implemented to infer the optimal set of parameters  $\boldsymbol{\theta}_k^{(t)}$  of the energy function. A frame  $t$  is classified using the Bayes' theorem,

$$\begin{aligned} p\left(y^{(t)} = K \mid \mathbf{X}^{(t)}, \boldsymbol{\theta}_k^{(t)}, \alpha_k\right) &= \frac{p\left(\mathbf{X}^{(t)} \mid \boldsymbol{\theta}_k^{(t)}, \alpha_k\right) p\left(y^{(t-1)} = K\right)}{p\left(\mathbf{X}^{(t)}\right)} \\ &\propto p\left(\mathbf{X}^{(t)} \mid \boldsymbol{\theta}_k^{(t)}, \alpha_k\right) p\left(y^{(t-1)} = K\right). \end{aligned} \quad (45)$$

The likelihood function is factorized to infer the distribution of each feature independently,

$$p\left(\mathbf{x}_1^{(t)}, \mathbf{x}_2^{(t)} \mid \boldsymbol{\theta}_k^{(t)}, \alpha_k\right) = p\left(\mathbf{x}_1^{(t)} \mid \boldsymbol{\theta}_{1,k}^{(t)}, \alpha_k\right) p\left(\mathbf{x}_2^{(t)} \mid \boldsymbol{\theta}_{2,k}^{(t)}, \alpha_k\right) \quad (46)$$

where  $\boldsymbol{\theta}^{(t)} = \{\boldsymbol{\theta}_1^{(t)}, \boldsymbol{\theta}_2^{(t)}\}$  are the parameters of the likelihood distributions, and  $\alpha_k$  the prior of the cluster weight.

The log-likelihood of a number of clusters  $K$  is defined as the likelihood of a mixture model. The class  $y^{(t)}$  is the number of cluster  $K$  in the mixture model. The parameters of the mixture model were inferred using the features extracted  $\mathbf{x}^{(t)}$  from frame  $t$ ,

$$\varphi\left(\mathbf{x}_i^{(t)}, y^{(t)} = K\right) \triangleq \sum_{k=1}^K \log \left[ \gamma_{i,k}^{(t)} p\left(\mathbf{x}_i^{(t)} \mid \hat{\boldsymbol{\theta}}_k^{(t)}, \hat{\alpha}_k\right) \right]. \quad (47)$$

where  $\hat{\boldsymbol{\theta}}^{(t)}$  are the set of parameters that maximize the complete data log-likelihood of the mixture model with  $K$  clusters, and  $\hat{\alpha}_k$  is the optimal prior. The prior can be expressed as,

$$p\left(y^{(t-1)}\right) = \frac{1}{Z} \exp \left[ -\psi\left(y^{(t-1)}\right) \right], \quad (48)$$

and the potential function which is proposed for this problem, is a variation of the original 1-dimensional Ising model,

$$\psi\left(y^{(t)}, y^{(t-1)}\right) \triangleq \beta \delta\left(y^{(t)}, y^{(t-1)}\right) = \begin{cases} +1 & \text{if } y^{(t)} = y^{(t-1)} \\ -1 & \text{if } y^{(t)} \neq y^{(t-1)} \end{cases} \quad (49)$$

where  $\beta$  parameter has to be cross-validated.

By applying expression (47) and (48) in (45) and taking logarithms, the energy function for a frame  $t$  with class  $y^{(t)}$  and features  $\mathbf{x}_i^{(t)}$  results in

$$\mathcal{U}\left(y^{(t)} = K \mid \mathbf{X}^{(t)}, \hat{\boldsymbol{\theta}}_k^{(t)}, \hat{\alpha}_k\right) = \sum_{k=1}^K \sum_{i=1}^N \log \left[ \gamma_{i,k}^{(t)} p\left(\mathbf{x}_i^t \mid \hat{\boldsymbol{\theta}}_k^{(t)}, \hat{\alpha}_k\right) \right] + \psi\left(y^{(t)}\right). \quad (50)$$

plus constant terms, this is, one can say that  $p(y^{(t)} = K \mid \mathbf{X}^{(t)}, \hat{\boldsymbol{\theta}}_k^{(t)}, \hat{\alpha}_k)$  is proportional to  $\exp[\mathcal{U}(y^{(t)} = K \mid \mathbf{X}^{(t)}, \hat{\boldsymbol{\theta}}_k^{(t)}, \hat{\alpha}_k)]$ .

A number of clusters  $K$  is assigned to a frame  $t$  by the MAP criterion,

$$\hat{y}^{(t)} = \operatorname{argmax}_k \mathcal{U}\left(y^{(t)} = K \mid \mathbf{X}^{(t)}, \hat{\boldsymbol{\theta}}_k^{(t)}, \hat{\alpha}_k\right). \quad (51)$$

### 3 Experiments

#### 3.1 Study Area and Data Acquisition System

The climate of Albuquerque is arid semi-continental with little precipitation, which is more likely during summer months. The average altitude of the city is 1,620m. Between mid May and mid June, the sky is clear or partly cloudy 80% of the time. Approximately 170 days of the year are sunny, with less than 30% cloud coverage, and 110 are partly sunny, with 40% to 80% cloud coverage. Temperatures range from a minimum of 268.71K in winter to a maximum of 306.48K in summer. Combined rainfall and snowfall are approximately 27.94cm per year.

The proposed detection methods utilize data acquired by a DAQ system equipped with a solar tracker that updates its pan, and tilt every second, maintaining the Sun in a central position in the images along a day. The IR sensor is a Lepton<sup>1</sup> radiometric camera with wavelength from 8 to 14  $\mu\text{m}$ . The pixels in a frame are temperature measurements in centikelvin. The resolution of the IR images is  $80 \times 60$  pixels. The DAQ is localized on the roof area of UNM-ECE building in Albuquerque, NM. The dataset composed of GSI measurements and IR images is available in a repository [89].

The weather features that were used to compute the clouds height as well as to remove cyclostationary artifacts on the IR images are: atmospheric pressure, air temperature, dew point and humidity. The weather station measures every 10 minutes. The data was interpolated to match the IR images samples. The weather station is located at the University of New Mexico Hospital. It is publicly accessible<sup>2</sup>.

#### 3.2 Image Preprocessing

The IR images were preprocessed first, to remove the effects of the direct irradiance from the Sun, and the scattered irradiance from the atmosphere. And second, to remove the scattered irradiance from the germanium IR camera window (see Fig. 1). The effect of the direct irradiance from Sun is constant on the IR images, thus it is modelled and removed. On the other hand, the scattering effect produced by the atmosphere is cyclostationary, so the optimal model in each frame is different. The parameters of atmospheric irradiance model depends on the azimuth and elevation angles of the Sun, and on weather features. The scattering effect produced by germanium IR camera window is modelled and removed using the median IR image of the last clear-sky images (see Fig. 2). The image processing methods and atmospheric conditions model are fully described in [75].

<sup>1</sup><https://www.flir.com/>

<sup>2</sup><https://www.wunderground.com/dashboard/pws/KNMALBUQ473>

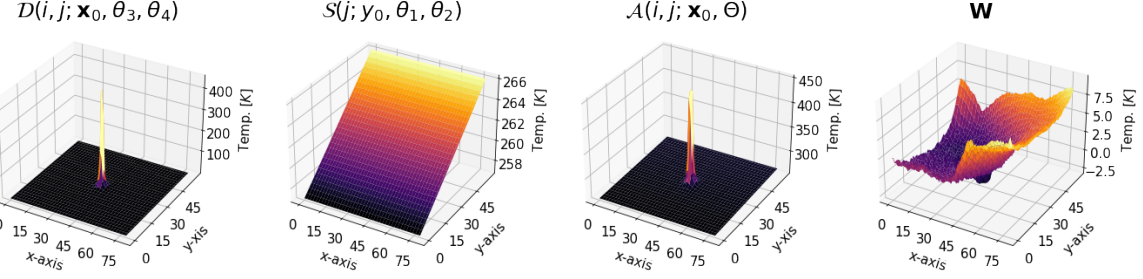


Figure 1: Irradiance effect models applied in the image preprocessing. From left to right, direct irradiance effect of the Sun, scattering effect produced by the atmosphere, and combination of the irradiance effects of the Sun and the atmosphere, and scattering effect produced by the germanium camera window.

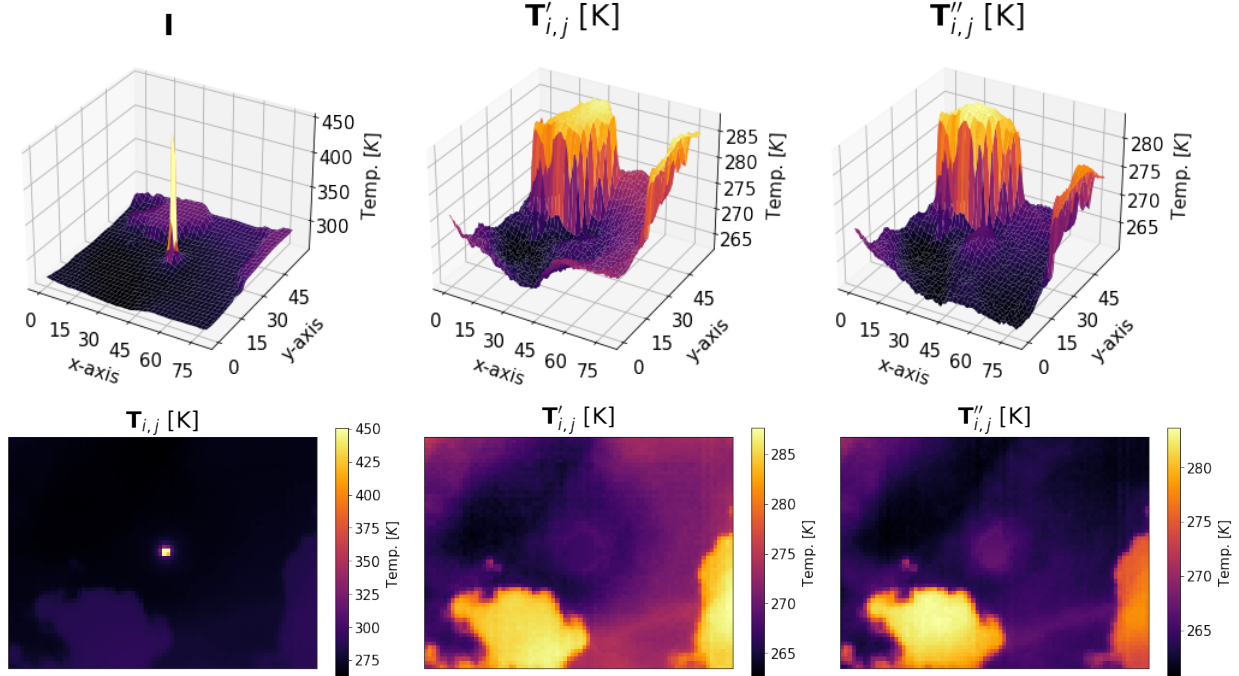


Figure 2: Preprocessing of the IR images. The images in the first row show the 3-dimensional image of the images in the second row. From left to right, raw IR image, IR after removing the effects of the atmospheric irradiance, and IR after removing the effects of the atmospheric irradiance and the scattering effect produced by the camera window. The models applied are shown in Fig. 1.

The proposed algorithm for the detection of clouds in multiple wind velocity fields, requires that the pixels with a cloud were previously segmented in the images. In this way, only features from pixels with clouds are analyzed. The cloud segmentation algorithm implemented in this investigation is a voting scheme that uses three different cloud segmentation models. The segmentation models are a Gaussian process, a support vector machine and unsupervised MRF (see Fig. 3). The cloud segmentation models and feature extraction are explained in [53].

### 3.3 Parameters Cross-Validation

The parameters that have to be cross-validated for each mixture model are  $\alpha_k$  and  $\beta$ . The parameter  $\alpha_k$  in Eq. (17) is the parameter of the prior distribution of the cluster weight  $\pi_k$  in a mixture model. The parameters  $\alpha$  in a mixture model of the temperatures are cross-validated as  $\alpha \triangleq \alpha_0 \mathbf{I}_{K \times 1}$  for simplification. Equivalently, the parameters  $\alpha$  in a mixture model of the velocity vectors are cross-validated as  $\alpha \triangleq \alpha_0 \mathbf{I}_{K \times 1}$ . The parameter  $\beta$  in Eq. (49) is the prior of the number of cloud layers in an image used in the temporal MRF.

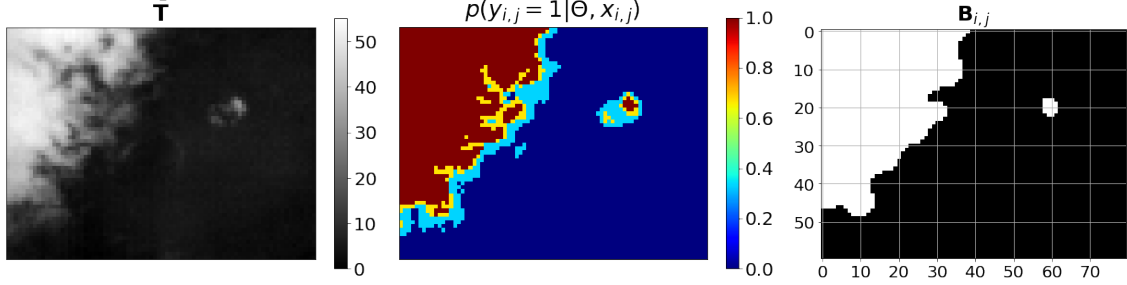


Figure 3: Cloud segmentation in IR images. The first image shows the IR normalized to 8bits, the second images shows the probabilities computed by the segmentation algorithm of pixel having a cloud, and the third images shows the segmentation after applied a  $\geq 0.5$  threshold to the probabilities. The normalized images are also used to compute the velocity vectors in the proposed WPLK.

Multiple Cloud Layers Detection Accuracy [%]										
Univariate Likelihoods	$\mathcal{L}$	Bayesian Metrics				Cross-Validated		MAP-MRF		
		$\mathcal{BIC}$	$\mathcal{AIC}$	$\mathcal{CLC}$	$\mathcal{ICL}$	$\alpha_0$	$\alpha_1$	$\beta$	$\psi(y^{(t)} = y^{(t-1)})$	
$\mathcal{B}(\bar{T}_{i,j})$		66.67	70.74	70.74	76.3	76.67	1	-	200	75.93
$\mathcal{G}(\bar{T}_{i,j})$		60	61.11	60.74	66.67	70.74	1	-	300	53.55
$\mathcal{N}(T_{i,j})$		<b>74.07</b>	<b>73.7</b>	<b>71.85</b>	<b>79.63</b>	<b>81.11</b>	100	-	500	<b>87.41</b>
$\mathcal{VM}(\phi_{i,j})$		57.41	60.37	61.85	58.52	61.11	-	1	500	60
$\mathcal{G}(r_{i,j})$		41.48	40.37	42.22	39.63	36.67	-	10	1000	37.78
$\mathcal{N}(\mathbf{v}_{i,j})$		65.93	68.15	67.04	69.63	67.41	-	100	600	61.85

Table 1: Detection accuracy achieved when univariate probability functions are used in a mixture model likelihood. The detection accuracy is compared using different Bayesian metrics and a mixture model with a prior on the weights and the clusters number.

The parameters cross-validation was implemented in a High Performances Computer (HPC). Even when the parameters cross-validation is implemented in a HPC, it is still computationally expensive and the number of validation samples is prohibitive. The parameters cross-validation used two nodes and was distributed across sixteen cores, which corresponds with the number of possible  $\beta$  in the cross-validation  $\beta = \{0, \dots, 1000\}$ . In each core, all possible combinations of  $\alpha_0$  (temperature clusters prior) and  $\alpha_1$  (velocity vectors clusters prior) were cross-validated  $\alpha_k = \{1, \dots, 1000\}$ . The performances of each combination of parameters for each mixture model were evaluated in the six training sequences. The optimal combination of parameters for each mixture model is which achieved the highest accuracy.

The training dataset is formed by six sequences of 21 consecutive images acquired on six different days. The training sequences were captured on different seasons and different times of the day. IR images were manually label as having one cloud layer  $K = 1$  or two cloud layers  $K = 2$ . The images from three of the six days show a layer of cirrusstratus in winter in the morning, altostratus in spring in the afternoon and stratocumulus in summer in the afternoon. The other three days show two layers of altostratus and stratocumulus in winter at noon, cirrusstratus and altocumulus in spring in the afternoon, and cirruscumulus and cumulus in summer in the morning. As the proposed method is an online machine learning algorithm, the training dataset is used only for prior distribution parameters cross-validation. The optimal parameters of the mixture models are computed for each new sample during the implementation.

### 3.4 Testing Performances

The testing dataset is composed of ten consecutive sequences of 30 images. The sequences were acquired at different hours of the day and in days that are from different seasons. The images in the testing dataset were acquired after the training dataset. The images in the testing dataset were manually label in the same way that training labels. The

Multiple Cloud Layers Detection Accuracy [%]										
Factorized Likelihood	Bayesian Metrics					Cross-Validated			MAP-MRF	
	$\mathcal{L}$	$BIC$	$AIC$	$CLC$	$ICL$	$\alpha_0$	$\alpha_1$	$\beta$	$\psi(y^{(t)} = y^{(t-1)})$	
$\mathcal{B}(\bar{T}_{i,j})\mathcal{V}\mathcal{M}(\phi_{i,j})$	68.89	68.89	69.63	<b>73.33</b>	<b>74.44</b>	1	10	650	<b>97.41</b>	
$\mathcal{B}(\bar{T}_{i,j})\mathcal{G}(r_{i,j})$	51.48	48.89	49.26	52.96	49.63	1	1000	650	69.26	
$\mathcal{V}\mathcal{M}(\phi_{i,j})\mathcal{G}(r_{i,j})$	51.11	48.52	48.15	42.22	43.70	-	10	1000	57.78	
$\mathcal{B}(\bar{T}_{i,j})\mathcal{V}\mathcal{M}(\phi_{i,j})\mathcal{G}(r_{i,j})$	55.19	55.19	55.56	57.41	56.3	10	100	1000	88.15	
$\mathcal{G}(\tilde{T}_{i,j})\mathcal{V}\mathcal{M}(\phi_{i,j})$	50.37	50.37	62.96	58.89	60	10	1	400	67.78	
$\mathcal{G}(\tilde{T}_{i,j})\mathcal{G}(r_{i,j})$	62.22	62.22	50	50.37	50.74	10	10	400	54.81	
$\mathcal{G}(\tilde{T}_{i,j})\mathcal{V}\mathcal{M}(\phi_{i,j})\mathcal{G}(r_{i,j})$	53.7	56.67	52.96	46.3	50.74	10	1	650	51.11	
$\mathcal{N}(T_{i,j})\mathcal{V}\mathcal{M}(\phi_{i,j})$	<b>78.15</b>	<b>76.67</b>	<b>77.41</b>	72.96	71.85	100	1000	600	85.93	
$\mathcal{N}(T_{i,j})\mathcal{G}(r_{i,j})$	64.07	66.67	64.44	61.85	70.37	1000	100	500	79.63	
$\mathcal{N}(T_{i,j})\mathcal{V}\mathcal{M}(\phi_{i,j})\mathcal{G}(r_{i,j})$	73.33	67.78	68.15	72.96	68.89	100	1	400	72.96	

Table 2: Detection accuracy achieved when the mixture model likelihood is factorized in the product of independent likelihoods functions for each feature. The detection accuracy is compared using different Bayesian metrics and adding a prior of the weights and the cloud layers number to mixture model.

Multiple Cloud Layers Detection Accuracy [%]										
Multivariate Likelihoods	Bayesian Metrics					Cross-Validated			MAP-MRF	
	$\mathcal{L}$	$BIC$	$AIC$	$CLC$	$ICL$	$\alpha_0$	$\alpha_1$	$\beta$	$\psi(y^{(t)} = y^{(t-1)})$	
$\mathcal{B}(\bar{T}_{i,j})\mathcal{N}(\mathbf{v}_{i,j})$	<b>70</b>	<b>71.11</b>	<b>70.37</b>	<b>75.56</b>	<b>75.93</b>	10	1000	650	<b>94.44</b>	
$\mathcal{G}(\tilde{T}_{i,j})\mathcal{N}(\mathbf{v}_{i,j})$	61.48	61.48	62.96	55.19	57.04	1	100	450	68.15	
$\mathcal{B}\mathcal{G}(\tilde{T}_{i,j}, r_{i,j})$	50	50.37	50.37	50	50.37	1	-	0	50.37	
$\mathcal{B}\mathcal{G}(\tilde{T}_{i,j}, r_{i,j})\mathcal{V}\mathcal{M}(\phi_{i,j})$	50	50.37	50	50	49.63	1	1	0	50	
$\mathcal{N}(T_{i,j}, \mathbf{v}_{i,j})$	52.22	52.96	52.22	51.85	64.44	100	-	1000	74.07	

Table 3: Detection accuracy achieved when multivariate probability functions are used in the likelihood of the mixture model. The detection accuracy is compared using different Bayesian metrics and a maximum a posterior implementation of a mixture model with a prior on the weights and cluster numbers.

testing dataset includes five sequences of images that have one layer of clouds, and five sequences of images that have two layers of clouds. The clouds in the sequences with one layer are: stratocumulus in summer morning, cumulus in summer morning, stratus in summer afternoon, cumulus in fall morning, and stratocumulus in winter at noon. The clouds in the sequences with two layers are: cumulus and cirrstratus in summer morning, cumulus and altostratus in fall at noon, cumulus and cirrus in fall afternoon, stratocumulus and altostratus in fall at noon, and cumulus and nimbustratus in winter afternoon.

We assume that the distribution of the velocity vectors is different in each cloud layers that appears in an IR image. In addition, we assume that exists a correlation between the height of a cloud and its velocity vectors. As the height of a cloud is a function on its temperature, so that we propose to use the temperature of the pixels and the velocity vector to infer the number of cloud layers in an IR image. The distribution of temperatures is inferred using a BMM, GaMM and GMM, see Fig. 4. The performances of each distribution are analyzed and compared in table 1. The posterior probabilities of the temperature mixture models in Fig 4, are the weights used in the WPLK.

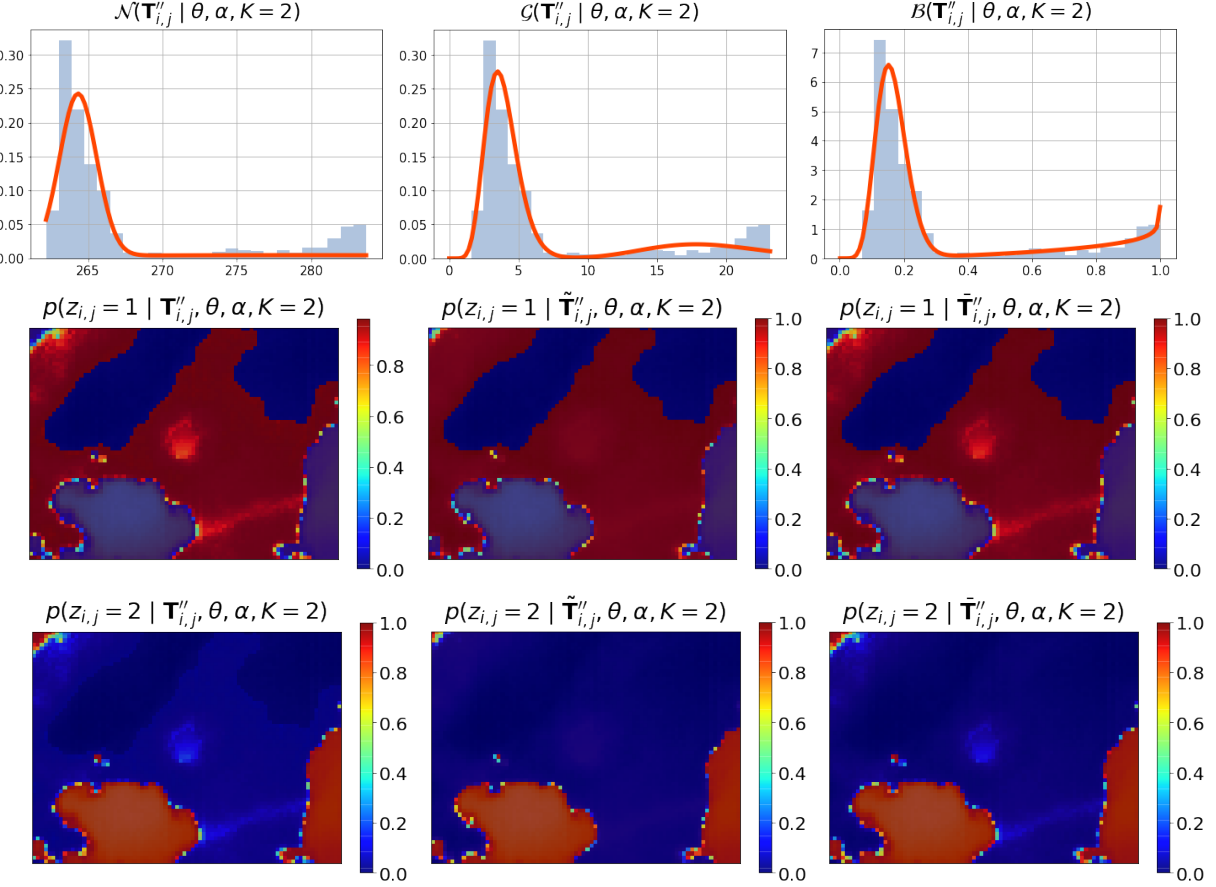


Figure 4: Distribution of the temperatures inferred using a GMM, GaMM and BeMM organized by columns. The mixture models likelihood evaluated with the optimal parameters. The mixture models posterior probabilities are shown row for the bottom cloud layer and the top cloud layer in the second and third respectively.

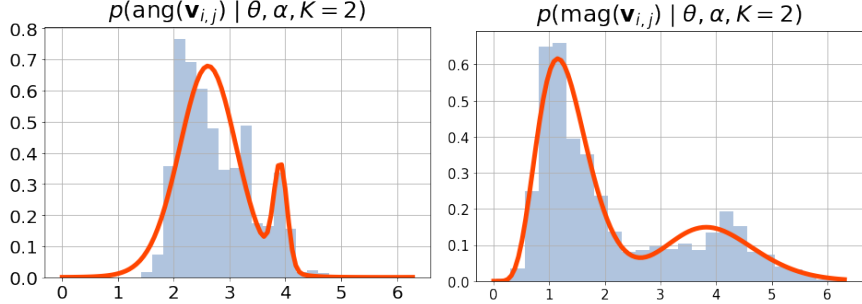


Figure 5: Distributions of the velocity vector angle, magnitude and x and y components. The distributions were inferred using a VMM, GaMM, multivariate GMM respectively. The first row shows the likelihoods, and the second and third row the posterior probabilities of the first and second cloud layer.

The distribution of the velocity vectors components is inferred using a multivariate GMM. The performances of the multivariate GMM are compared to the distribution of the velocity vectors magnitude and angle inferred factorizing the probability of the velocity vectors in two independent probabilities (see table 2 and 3). In Fig. 5, the distribution of the velocity vectors magnitude and are inferred using a GaMM and VMM respectively.

When weighted are not applied in the WPLK method, the distribution of the temperatures, velocity vectors angles and magnitude can be inferred using a multivariate GMM. Similarly, a DGMM is also proposed to inferred the distribution of the temperatures and velocity vectors magnitude. The multivariate GMM and DGMM likelihood are displayed in

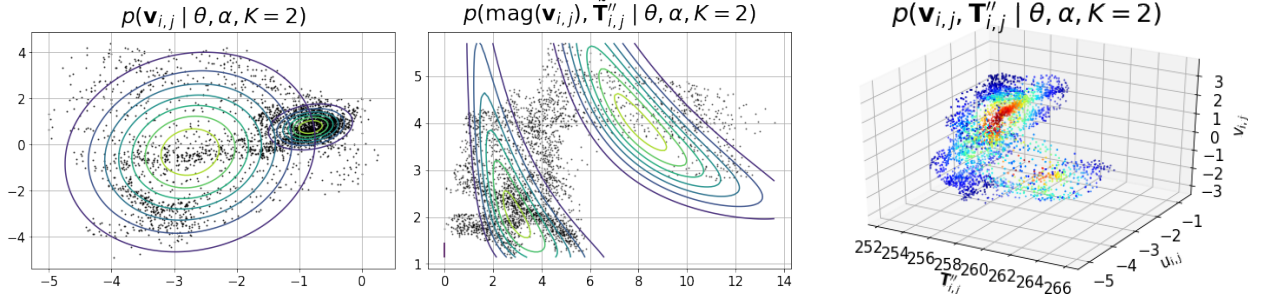


Figure 6: Joint distribution of the temperatures and the velocity vectors. The distribution using the temperatures and both velocity vectors components was inferred using multivariate GMM (top row). The Distribution of the temperatures and the magnitude of the velocity vectors was inferred using a BGaMM (bottom row). The posterior probabilities of each cloud layer are shown in the second and third column respectively.

Fig. 6. In this case, the probability of the velocity vector angles is factorized and an inferred independently using a VMMM. The performance of these two mixture models are also shown in table 3.

The experiments were carried out in the Wheeler high performances computer of UNM-CARC, which uses SGI AltixXE Xeon X5550 at 2.67GHz with 6 GB of RAM memory per core, has 8 cores per node, 304 nodes total, and runs at 25 theoretical peak FLOPS. It has installed Linux CentOS 7. The DAQ is localized on the roof area of UNM-ME building in Albuquerque, NM.

## 4 Discussion

In our problem at hands, the BIC and AIC criteria does not produce an improvements on the detection accuracy with respect to accuracy achieved by ML criteria. The best detection accuracy achieved by a model that uses the ML criteria is 78.15%. In contrast, the same model achieved a detection accuracy of 76.67% and 77.41% when the criteria was minimum BIC and AIC respectively (see table 2). This mixture model have a factorized likelihood that uses a normal probability function to infer the temperatures distribution and a Von Mises to infer the velocity vectors angles. However, when the minimum CLC and ICL criteria are applied the detection accuracy improved with respect to that achieved by the ML criteria. The detection accuracy achieved by CLC, ICL and ML criteria was 81.11%, 79.63% and 74.07% respectively (see table 1). Therefore, the best detection using a Bayesian metric was performed by a mixture model with a normal likelihood on the temperatures.

The detection accuracy of the proposed algorithms increases when the mixture model includes prior distributions on mixture weights and the cluster number. In this mixture models the decision criteria is MAP. In tables 1-3, when we look the model that achieved the best detection accuracy using a Bayesian metric (ICL), the detection accuracy increased from 81.11% to 87.11%. Nevertheless, the best detection accuracy using the MAP criteria reach 97.41% (see table 2). The model which presents the best detection accuracy is a MAP mixture model with factorized likelihood that uses a beta probability distribution to infer the temperature distribution and a Von Mises to infer that of the velocity vectors angles.

The results shows that is feasible to identify different cloud layers in IR ground-based sky-images, see Fig. 7-9. The main advantage of this algorithm is that it provides the capability of independently estimate motion of different cloud layers in an IR image using the posterior probabilities in Fig. 4. This is useful to predict when different clouds will occlude the Sun. The features and dynamics can be analyzed independently to increase the performances of a solar forecasting algorithm. Another advantage of the learning algorithm proposed is unsupervised so the user does not need to provide labels, which makes the training process less labour intensive.

The Bayesian metrics are not useful in this application. The highest accuracy achieved by a Bayesian metric was 81.11% with a GMM of the temperatures. The model selection was performed using minimum ICL criteria. The performances of the BGaMM are lower than the rest of the mixture models, thus it is not practical to assess the number of cloud layers in IR images. This is because the BGaMM tends to overfit even when cluster weights are regularized using a prior distribution.

A disadvantage of the proposed unsupervised learning algorithm is that to guaranty that the EM algorithm converges to a local maxima, the EM may require several initialization. This is problematic when the cloud layer detection algorithms

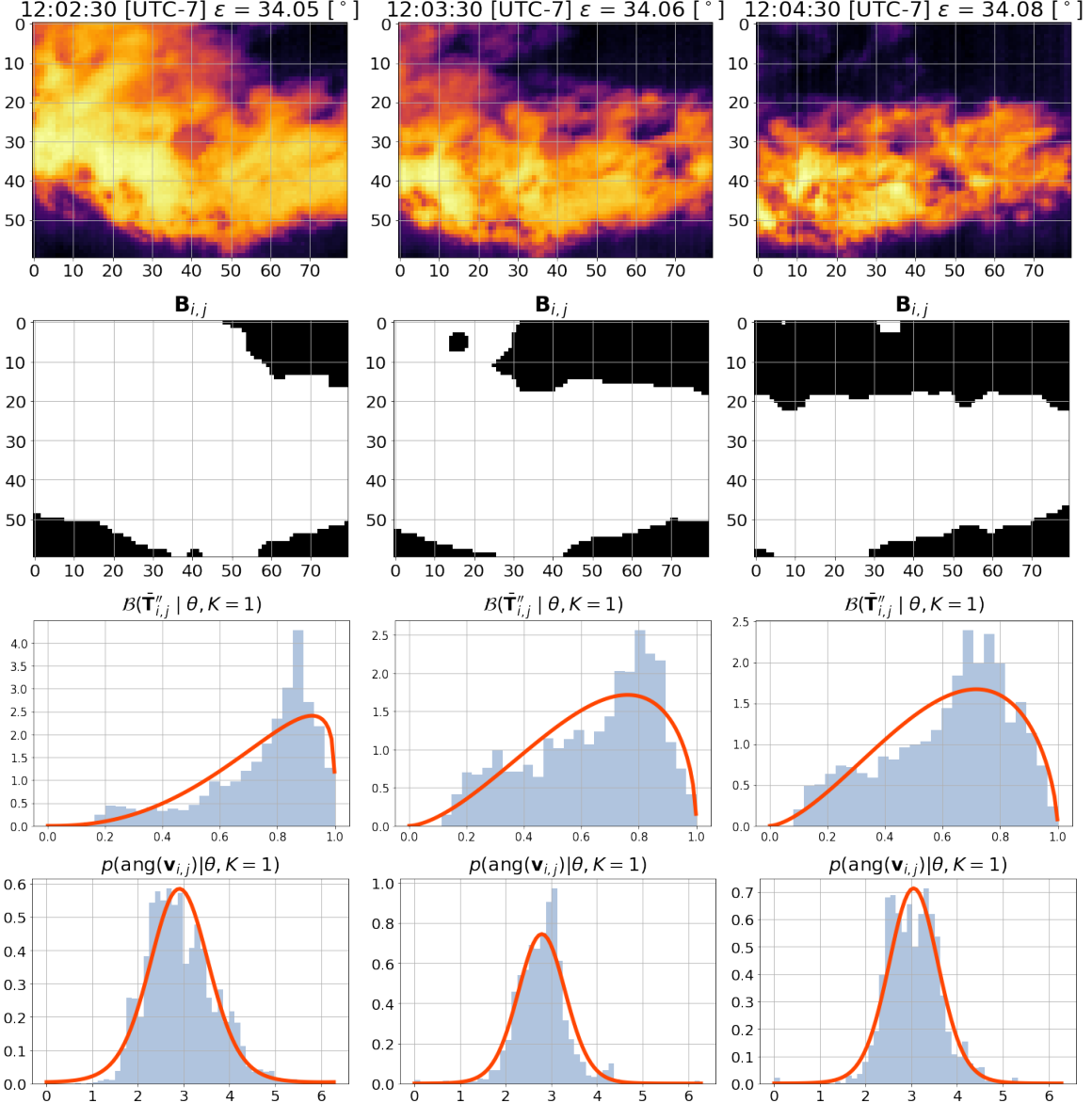


Figure 7: Testing sequence of consecutive IR images acquired at 1 minute interval. In the first row, the IR images show a cloud flowing a single detected wind velocity field. The images in the second row show the cloud segmentation. The graphs in the third and fourth row shows the selected model distribution of the temperatures and the velocity vectors angles respectively.

is meant for real-time applications. An implementation of the algorithm feasible in real-time applications will require multiple CPUs to run the different initialization in parallel.

## 5 Conclusions

This investigation proposed an online unsupervised learning algorithm to detect moving clouds in different wind velocity fields. The mixture model of pixel temperature used to know when a cloud is below or on top of another. The posterior probabilities of the mixture model are used to compute velocity vectors. The algorithm to compute the velocity vectors is a weighted pyramidal implementation of the Lucas-Kanade optical flow. The weights are the posterior probabilities of the mixture model. The velocity vectors are computed in the scenario that there is one cloud layer and in the scenario that there are two cloud layers (using the cloud segmentation or the posterior probabilities respectively). The distribution

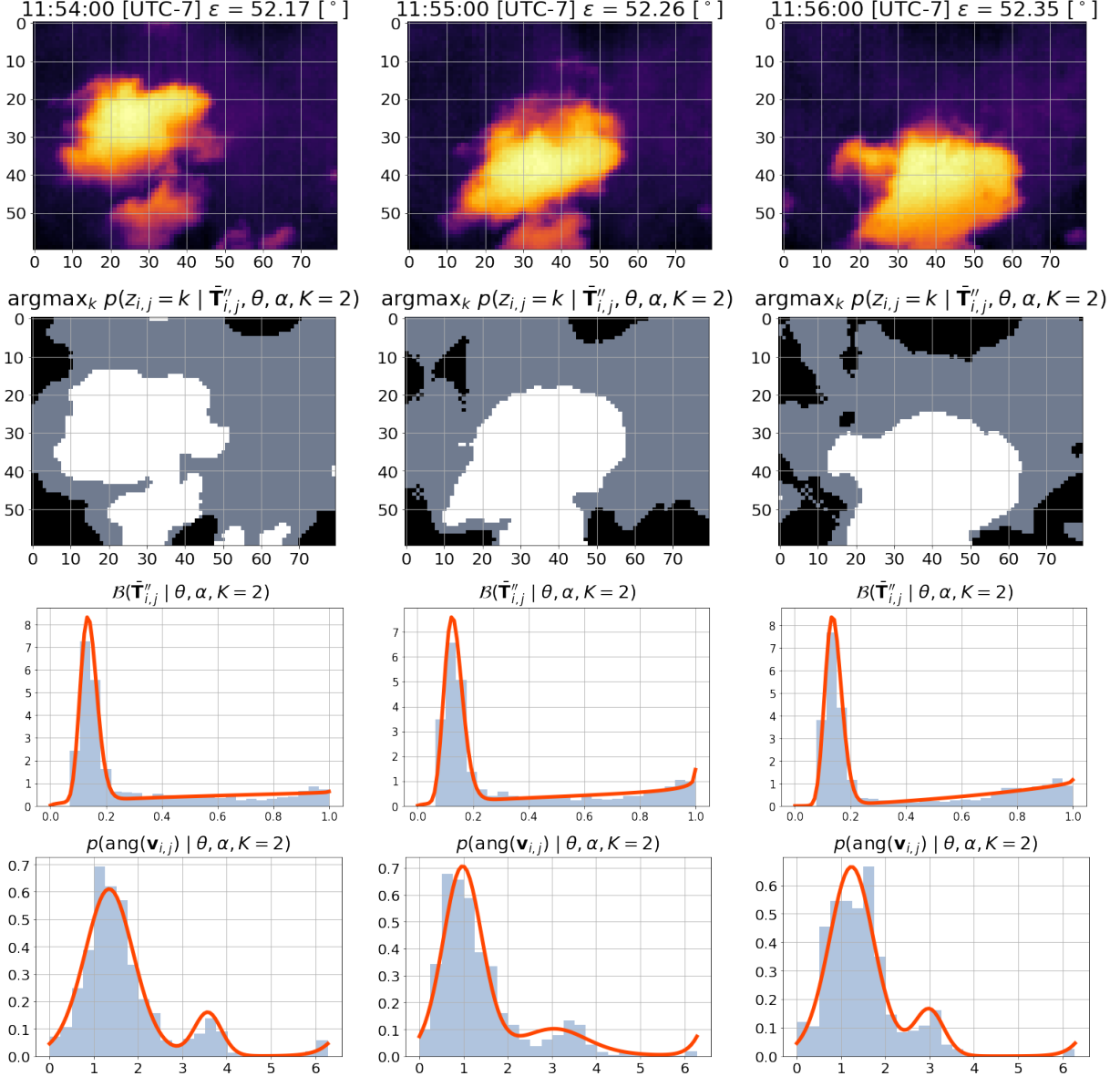


Figure 8: Testing sequence of IR images with detected two cloud layers (first row). The time interval between images is 1 minutes. The images in second row shows the pixels that belong to the low and high temperatures in gray and white respectively. The pixels in black were classified as no having a cloud by the segmentation algorithm. The third and fourth row show the distribution of the temperature and velocity vectors of the best model.

of the velocity vectors and the temperatures is used to determined which of analyzed scenarios is the most likely. The proposed algorithm implements the maximum a posteriori criteria.

The detection of clouds flowing in different wind velocity field is useful to increase the accuracy of a forecasting algorithm that predicts the global solar irradiance that will reach a photovoltaic power plant. The prediction will aid a smart grid to adjust the generation mix to compensate the decrease of energy generated by the photovoltaic panels.

In particular, the posterior probabilities of the pixels temperatures may aid the extraction of features using either using image processing techniques, gradient-based learning (e.g. deep neural networks) or both. However, the posterior probabilities are only advantageous when there are multiple cloud layers in an IR image. The proposed method models a includes a prior distribution of the cluster weight, and prior function of each possible scenario. The prior function of the scenarios is a temporal implementation of Markov Random Field. The proposed method is capable of correctly detecting when clouds are moving in different wind velocity fields. This investigation shows that the proposed method

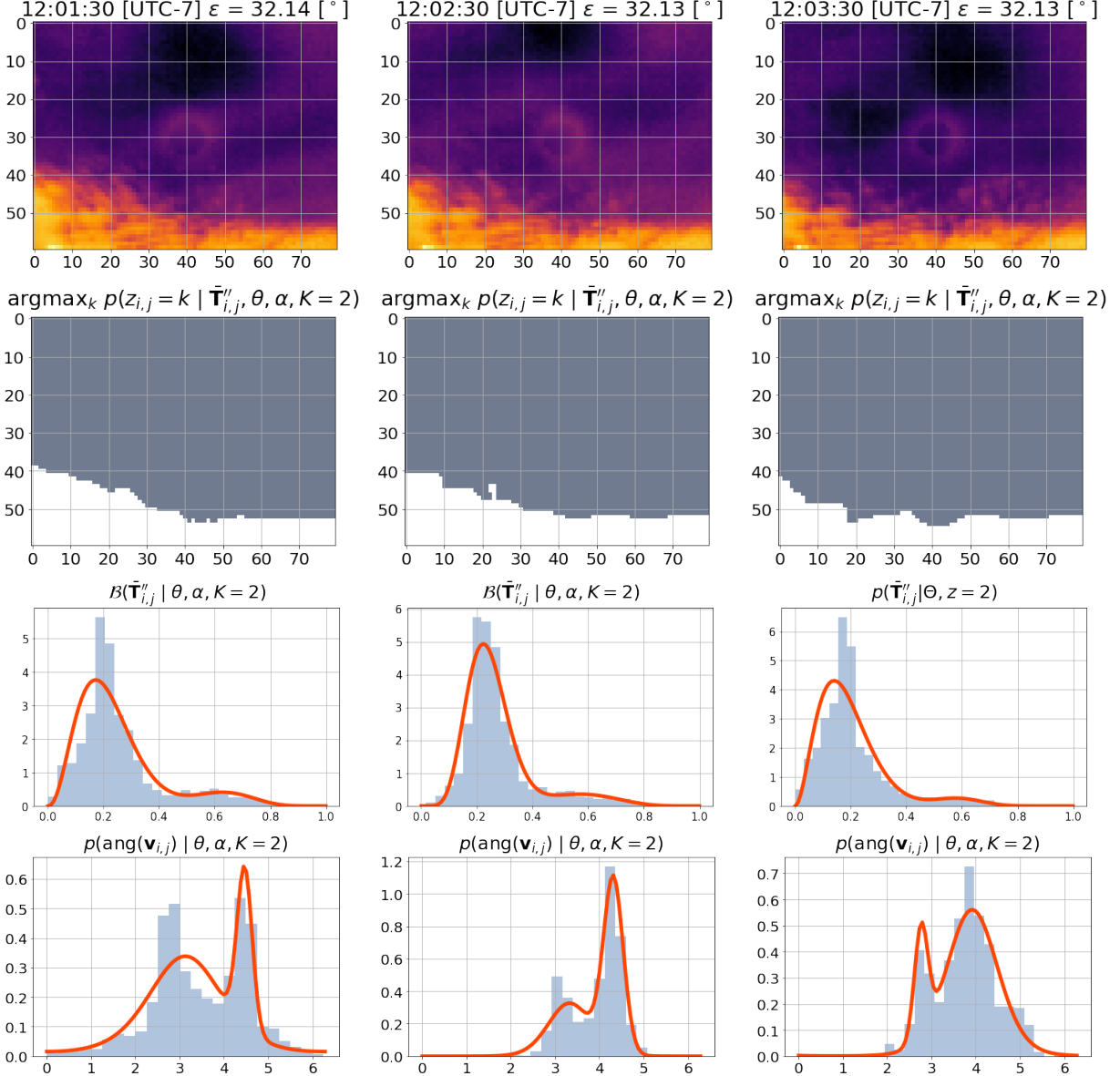


Figure 9: Testing image with two detected cloud layers layers. The time interval between the IR image is 1 minute. The consecutive IR images are shown in the first row. The pixel labels of the top (grey) or the bottom cloud layer (white) are shown in the second row. The third and fourth row show the factorized likelihood that uses a VMM and GaMM for the velocity vectors angles and magnitude respectively.

increases the detection accuracy compared to the accuracy achieved by the most common Bayesian metrics used in practice.

Future work in this area will implement the cloud detection algorithm in a ramp-down and intra-hour solar forecasting algorithms. The dynamics of clouds may be analyzed independently to extract features from clouds moving in different wind velocity fields. The improvement in the performances can be assessed to determine how to combine the features extracted from different clouds to model their respective influence on the GSI that will reach the surface of a photovoltaic system. Another investigation may focus on the implementation of the proposed algorithm in images acquired using ground-based all-sky imagers that are sensible to the visible light spectrum instead of the infrared. The most interesting aspect will be to fusion information acquired using visible and infrared light cameras.

## 6 Acknowledgments

This work has been supported by NSF EPSCoR grant number OIA-1757207 and the King Felipe VI endowed Chair. Authors would like to thank the UNM Center for Advanced Research Computing, supported in part by the National Science Foundation, for providing the high performance computing and large-scale storage resources used in this work.

## References

- [1] Ning Zhao and Fengqi You. Can renewable generation, energy storage and energy efficient technologies enable carbon neutral energy transition? *Applied Energy*, 279:115889, 2020.
- [2] Ehsanul Kabir, Pawan Kumar, Sandeep Kumar, Adedeji A. Adelodun, and Ki-Hyun Kim. Solar energy: Potential and future prospects. *Renewable and Sustainable Energy Reviews*, 82:894 – 900, 2018.
- [3] Cheng Feng, Yi Wang, Qixin Chen, Yi Ding, Goran Strbac, and Chongqing Kang. Smart grid encounters edge computing: opportunities and applications. *Advances in Applied Energy*, 1:100006, 2021.
- [4] Kenji Otani, Jyunya Minowa, and Kosuke Kurokawa. Study on areal solar irradiance for analyzing areally-totalized pv systems. *Solar Energy Materials and Solar Cells*, 47(1):281 – 288, 1997.
- [5] Kari Lappalainen, Anssi Mäki, and Seppo Valkealahti. Effects of the sharpness of shadows on the mismatch losses of pv generators under partial shading conditions caused by moving clouds. In *Proceedings of 28th European photovoltaic solar energy conference*, pages 4081–4086, 2013.
- [6] Kari Lappalainen and Seppo Valkealahti. Output power variation of different pv array configurations during irradiance transitions caused by moving clouds. *Applied energy*, 190:902–910, 2017.
- [7] Luis Martín, Luis F. Zarzalejo, Jesús Polo, Ana Navarro, Ruth Marchante, and Marco Cony. Prediction of global solar irradiance based on time series analysis: Application to solar thermal power plants energy production planning. *Solar Energy*, 84(10):1772 – 1781, 2010.
- [8] R. Ahmed, V. Sreeram, Y. Mishra, and M.D. Arif. A review and evaluation of the state-of-the-art in pv solar power forecasting: Techniques and optimization. *Renewable and Sustainable Energy Reviews*, 124:109792, 2020.
- [9] Hao Quan and Dazhi Yang. Probabilistic solar irradiance transposition models. *Renewable and Sustainable Energy Reviews*, 125:109814, 2020.
- [10] Gilberto Figueiredo, Marcelo Pinho Almeida, Alex R.A. Manito, and Roberto Zilles. Assessment of an early degraded pv generator. *Solar Energy*, 189:385 – 388, 2019.
- [11] Ken ichi Shimose, Hideaki Ohtake, Joao Gari da Silva Fonseca, Takumi Takashima, Takashi Oozeki, and Yoshinori Yamada. Improvement of the japan meteorological agency meso-scale model for the forecasting the photovoltaic power production: Modification of the cloud scheme. *Energy Procedia*, 57:1346 – 1353, 2014. 2013 ISES Solar World Congress.
- [12] Björn Wolff, Jan Kühnert, Elke Lorenz, Oliver Kramer, and Detlev Heinemann. Comparing support vector regression for pv power forecasting to a physical modeling approach using measurement, numerical weather prediction, and cloud motion data. *Solar Energy*, 135:197 – 208, 2016.
- [13] Huaizhi Wang, Haiyan Yi, Jianchun Peng, Guibin Wang, Yitao Liu, Hui Jiang, and Wenxin Liu. Deterministic and probabilistic forecasting of photovoltaic power based on deep convolutional neural network. *Energy Conversion and Management*, 153:409 – 422, 2017.
- [14] Abinet Tesfaye Eseye, Jianhua Zhang, and Dehua Zheng. Short-term photovoltaic solar power forecasting using a hybrid wavelet-psosvm model based on scada and meteorological information. *Renewable Energy*, 118:357 – 367, 2018.
- [15] Fei Wang, Zhiming Xuan, Zhao Zhen, Yu Li, Kangping Li, Liqiang Zhao, Miadreza Shafie-khah, and João P.S. Catalão. A minutely solar irradiance forecasting method based on real-time sky image-irradiance mapping model. *Energy Conversion and Management*, 220:113075, 2020.
- [16] Steven D. Miller, Matthew A. Rogers, John M. Haynes, Manajit Sengupta, and Andrew K. Heidinger. Short-term solar irradiance forecasting via satellite/model coupling. *Solar Energy*, 168:102 – 117, 2018. Advances in Solar Resource Assessment and Forecasting.
- [17] Eugenia Kalnay. *Atmospheric Modeling, Data Assimilation and Predictability*. Cambridge University Press, 2003.
- [18] D. Lamb and J. Verlinde. *Physics and Chemistry of Clouds*. Cambridge University Press, 2011.
- [19] Tore Wizelius. *Developing wind power projects: theory and practice*. Earthscan, 2007.

[20] T. Wizelius. 2.13 - design and implementation of a wind power project. In Ali Sayigh, editor, *Comprehensive Renewable Energy*, pages 391 – 430. Elsevier, Oxford, 2012.

[21] Robert J. Charlson. 7 - the atmosphere. In Michael C. Jacobson, Robert J. Charlson, Henning Rodhe, and Gordon H. Orians, editors, *Earth System Science*, volume 72 of *International Geophysics*, pages 132 – 158. Academic Press, 2000.

[22] Olivier Bousquet, Pierre Tabary, and Jacques Parent du Châtelet. On the value of operationally synthesized multiple-doppler wind fields. *Geophysical research letters*, 34(22), 2007.

[23] Olivier Bousquet, Pierre Tabary, and Jacques Parent du Châtelet. Operational multiple-doppler wind retrieval inferred from long-range radial velocity measurements. *Journal of applied meteorology and climatology*, 47(11):2929–2945, 2008.

[24] Guillermo Terrén-Serrano and Manel Martínez-Ramón. Multi-layer wind velocity field visualization in infrared images of clouds for solar irradiance forecasting. *Applied Energy*, 288:116656, 2021.

[25] Patrick Mathiesen and Jan Kleissl. Evaluation of numerical weather prediction for intra-day solar forecasting in the continental united states. *Solar Energy*, 85(5):967 – 977, 2011.

[26] Richard Perez, Elke Lorenz, Sophie Pelland, Mark Beauharnois, Glenn Van Knowe, Karl Hemker, Detlev Heinemann, Jan Remund, Stefan C. Müller, Wolfgang Traunmüller, Gerald Steinmauer, David Pozo, Jose A. Ruiz-Arias, Vicente Lara-Fanego, Lourdes Ramirez-Santigosa, Martin Gaston-Romero, and Luis M. Pomares. Comparison of numerical weather prediction solar irradiance forecasts in the us, canada and europe. *Solar Energy*, 94:305 – 326, 2013.

[27] Patrick Mathiesen, Craig Collier, and Jan Kleissl. A high-resolution, cloud-assimilating numerical weather prediction model for solar irradiance forecasting. *Solar Energy*, 92:47 – 61, 2013.

[28] Remco A. Verzijlbergh, Petra W. Heijnen, Stephan R. de Roode, Alexander Los, and Harm J.J. Jonker. Improved model output statistics of numerical weather prediction based irradiance forecasts for solar power applications. *Solar Energy*, 118:634 – 645, 2015.

[29] L. Mazorra Aguiar, B. Pereira, P. Lauret, F. Díaz, and M. David. Combining solar irradiance measurements, satellite-derived data and a numerical weather prediction model to improve intra-day solar forecasting. *Renewable Energy*, 97:599 – 610, 2016.

[30] Akinobu Murata, Hideaki Ohtake, and Takashi Oozeki. Modeling of uncertainty of solar irradiance forecasts on numerical weather predictions with the estimation of multiple confidence intervals. *Renewable Energy*, 117:193 – 201, 2018.

[31] O. García-Hinde, G. Terrén-Serrano, M.Á. Hombrados-Herrera, V. Gómez-Verdejo, S. Jiménez-Fernández, C. Casanova-Mateo, J. Sanz-Justo, M. Martínez-Ramón, and S. Salcedo-Sanz. Evaluation of dimensionality reduction methods applied to numerical weather models for solar radiation forecasting. *Engineering Applications of Artificial Intelligence*, 69:157 – 167, 2018.

[32] Franco Marchesoni-Acland and Rodrigo Alonso-Suárez. Intra-day solar irradiation forecast using rls filters and satellite images. *Renewable Energy*, 161:1140 – 1154, 2020.

[33] R. Alonso-Suárez, M. David, V. Branco, and P. Lauret. Intra-day solar probabilistic forecasts including local short-term variability and satellite information. *Renewable Energy*, 158:554 – 573, 2020.

[34] H. S. Jang, K. Y. Bae, H. S. Park, and D. K. Sung. Solar power prediction based on satellite images and support vector machine. *IEEE Transactions on Sustainable Energy*, 2016.

[35] Lakshmi Mallika I, D. Venkata Ratnam, Saravana Raman, and G. Sivaraprasad. Machine learning algorithm to forecast ionospheric time delays using global navigation satellite system observations. *Acta Astronautica*, 173:221 – 231, 2020.

[36] M Cervantes, H Krishnaswami, W Richardson, and R Vega. Utilization of low cost, sky-imaging technology for irradiance forecasting of distributed solar generation. In *2016 IEEE Green Technologies Conference (GreenTech)*, pages 142–146. IEEE, 2016.

[37] Walter Richardson, Hariharan Krishnaswami, Rolando Vega, and Michael Cervantes. A low cost, edge computing, all-sky imager for cloud tracking and intra-hour irradiance forecasting. *Sustainability*, 9(4):482, 2017.

[38] Weicong Kong, Youwei Jia, Zhao Yang Dong, Ke Meng, and Songjian Chai. Hybrid approaches based on deep whole-sky-image learning to photovoltaic generation forecasting. *Applied Energy*, 280:115875, 2020.

[39] Yinghao Chu, Mengying Li, and Carlos F.M. Coimbra. Sun-tracking imaging system for intra-hour dni forecasts. *Renewable Energy*, 96:792 – 799, 2016.

[40] A. Mammoli, A. Ellis, A. Menicucci, S. Willard, T. Caudell, and J. Simmins. Low-cost solar micro-forecasts for pv smoothing. In *2013 1st IEEE Conference on Technologies for Sustainability (SusTech)*, pages 238–243, 2013.

[41] M. Caldas and R. Alonso-Suárez. Very short-term solar irradiance forecast using all-sky imaging and real-time irradiance measurements. *Renewable Energy*, 143:1643 – 1658, 2019.

[42] Peter Shaffery, Aron Habte, Marcos Netto, Afshin Andreas, and Venkat Krishnan. Automated construction of clear-sky dictionary from all-sky imager data. *Solar Energy*, 212:73 – 83, 2020.

[43] Chi Wai Chow, Bryan Urquhart, Matthew Lave, Anthony Dominguez, Jan Kleissl, Janet Shields, and Byron Washom. Intra-hour forecasting with a total sky imager at the uc san diego solar energy testbed. *Solar Energy*, 85(11):2881 – 2893, 2011.

[44] Joseph A Shaw and Paul W Nugent. Physics principles in radiometric infrared imaging of clouds in the atmosphere. *European Journal of Physics*, 34(6):S111–S121, oct 2013.

[45] Joseph A. Shaw, Paul W. Nugent, Nathan J. Pust, Brentha Thurairajah, and Kohei Mizutani. Radiometric cloud imaging with an uncooled microbolometer thermal infrared camera. *Opt. Express*, 13(15):5807–5817, Jul 2005.

[46] B. Thurairajah and J. A. Shaw. Cloud statistics measured with the infrared cloud imager (ici). *IEEE Transactions on Geoscience and Remote Sensing*, 43(9):2000–2007, Sep. 2005.

[47] Paul W. Nugent, Joseph A. Shaw, and Sabino Piazzolla. Infrared cloud imaging in support of earth-space optical communication. *Opt. Express*, 17(10):7862–7872, May 2009.

[48] Guillermo Terrén-Serrano and Manel Martínez-Ramón. Data acquisition and image processing for solar irradiance forecast, 2020.

[49] Nathan J. Pust Paul W. Nugent, Joseph A. Shaw. Correcting for focal-plane-array temperature dependence in microbolometer infrared cameras lacking thermal stabilization. *Optical Engineering*, 52(6):1 – 8 – 8, 2013.

[50] Andrea Mammoli, Guillermo Terrén-Serrano, Anthony Menicucci, Thomas P Caudell, and Manel Martínez-Ramón. An experimental method to merge far-field images from multiple longwave infrared sensors for short-term solar forecasting. *Solar Energy*, 187:254–260, 2019.

[51] Hehe Ren, Shujin Laima, Wen-Li Chen, Bo Zhang, Anxin Guo, and Hui Li. Numerical simulation and prediction of spatial wind field under complex terrain. *Journal of Wind Engineering and Industrial Aerodynamics*, 180:49 – 65, 2018.

[52] H. Escrig, Francisco Batlles, Joaquín Alonso-Montesinos, F.M. Baena, Juan Bosch, I. Salbidegoitia, and Juan Burgaleta. Cloud detection, classification and motion estimation using geostationary satellite imagery for cloud cover forecast. *Energy*, 55, 06 2013.

[53] Guillermo Terrén-Serrano and Manel Martínez-Ramón. Comparative analysis of methods for cloud segmentation in infrared images, 2020.

[54] Geoffrey E Hinton, Terrence Joseph Sejnowski, Tomaso A Poggio, et al. *Unsupervised learning: foundations of neural computation*. MIT press, 1999.

[55] Trevor Hastie, Robert Tibshirani, and Jerome Friedman. *Unsupervised learning*. Springer, 2009.

[56] Ernst Ising. Beitrag zur Theorie des Ferromagnetismus. *Zeitschrift fur Physik*, 31(1):253–258, February 1925.

[57] Stan Z Li. *Markov random field modeling in image analysis*. Springer Science & Business Media, 2009.

[58] Stuart Geman and Christine Graffigne. Markov random field image models and their applications to computer vision. In *Proceedings of the international congress of mathematicians*, volume 1, page 2. Berkeley, CA, 1986.

[59] RJ Birgeneau, RA Cowley, G Shirane, and H Yoshizawa. Temporal phase transition in the three-dimensional random-field ising model. *Physical review letters*, 54(19):2147, 1985.

[60] Małgorzata Turalska, Bruce J West, and Paolo Grigolini. Temporal complexity of the order parameter at the phase transition. *Physical Review E*, 83(6):061142, 2011.

[61] Farid Melgani and Sebastiano B Serpico. A markov random field approach to spatio-temporal contextual image classification. *IEEE Transactions on Geoscience and Remote Sensing*, 41(11):2478–2487, 2003.

[62] Shunsuke Kamijo, Yasuyuki Matsushita, Katsushi Ikeuchi, and Masao Sakauchi. Occlusion robust tracking utilizing spatio-temporal markov random field model. In *Proceedings 15th International Conference on Pattern Recognition. ICPR-2000*, volume 1, pages 140–144. IEEE, 2000.

[63] B. D. Lucas and T. Kanade. An iterative image registration technique with an application to stereo vision, 1981.

[64] Chris Stauffer and W Eric L Grimson. Adaptive background mixture models for real-time tracking. In *Proceedings. 1999 IEEE Computer Society Conference on Computer Vision and Pattern Recognition (Cat. No PR00149)*, volume 2, pages 246–252. IEEE, 1999.

[65] Jia Chen and Chi-Keung Tang. Spatio-temporal markov random field for video denoising. In *2007 IEEE Conference on Computer Vision and Pattern Recognition*, pages 1–8. IEEE, 2007.

[66] Zhi Wei, Hongzhe Li, et al. A hidden spatial-temporal markov random field model for network-based analysis of time course gene expression data. *The Annals of applied statistics*, 2(1):408–429, 2008.

[67] Geoffrey J McLachlan and Kaye E Basford. *Mixture models: Inference and applications to clustering*, volume 38. M. Dekker New York, 1988.

[68] Geoffrey J McLachlan and David Peel. *Finite mixture models*. John Wiley & Sons, 2004.

[69] Christopher M. Bishop. *Pattern Recognition and Machine Learning*. Springer, 2006.

[70] Kevin P. Murphy. *Machine Learning: A Probabilistic Perspective*. The MIT Press, 2012.

[71] Matthew Stephens. Dealing with label switching in mixture models. *Journal of the Royal Statistical Society: Series B (Statistical Methodology)*, 62(4):795–809, 2000.

[72] Iyyanki V. Muralikrishna and Valli Manickam. Chapter fourteen - air pollution control technologies. In *Environmental Management*, pages 337 – 397. Butterworth-Heinemann, 2017.

[73] Berthold KP Horn and Brian G Schunck. Determining optical flow. *Artificial intelligence*, 17(1-3):185–203, 1981.

[74] Gunnar Farnebäck. Two-frame motion estimation based on polynomial expansion. *Image analysis*, pages 363–370, 2003.

[75] Guillermo Terrén-Serrano and Manel Martínez-Ramón. Processing of global solar irradiance and ground-based infrared sky images for very short-term solar forecasting, 2021.

[76] Simon Baker, Ralph Gross, Takahiro Ishikawa, and Iain Matthews. Lucas-kanade 20 years on: A unifying framework: Part 2. *International Journal of Computer Vision*, 56:221–255, 2003.

[77] Anders Hast. Simple filter design for first and second order derivatives by a double filtering approach. *Pattern Recognition Letters*, 42:65 – 71, 2014.

[78] H. Farid and E. P. Simoncelli. Differentiation of discrete multidimensional signals. *IEEE Transactions on Image Processing*, 13(4):496–508, 2004.

[79] P.R. Smith. Bilinear interpolation of digital images. *Ultramicroscopy*, 6(2):201 – 204, 1981.

[80] Sumen Sen, Rajan Lamichhane, and Norou Diawara. A bivariate distribution with conditional gamma and its multivariate form. *Journal of Modern Applied Statistical Methods*, 13:169–184, 11 2014.

[81] Alexandre K. W. Navarro, Jes Frellsen, and Richard E. Turner. The multivariate generalised von mises distribution: Inference and applications. In *Proceedings of the Thirty-First AAAI Conference on Artificial Intelligence*, AAAI’17, pages 2394–2400. AAAI Press, 2017.

[82] Siddharth Gopal and Yiming Yang. Von mises-fisher clustering models. In Eric P. Xing and Tony Jebara, editors, *Proceedings of the 31st International Conference on Machine Learning*, volume 32 of *Proceedings of Machine Learning Research*, pages 154–162. PMLR, 6 2014.

[83] Arindam Banerjee, Inderjit S. Dhillon, Joydeep Ghosh, and Suvrit Sra. Clustering on the unit hypersphere using von mises-fisher distributions. *J. Mach. Learn. Res.*, 6:1345–1382, December 2005.

[84] Yuan Ji, Chunlei Wu, Ping Liu, Jing Wang, and Kevin R Coombes. Applications of beta-mixture models in bioinformatics. *Bioinformatics*, 21(9):2118–2122, 2005.

[85] Gideon Schwarz. Estimating the dimension of a model. *Ann. Statist.*, 6(2):461–464, 03 1978.

[86] Hirotugu Akaike. A new look at the statistical model identification. *IEEE Transactions on Automatic Control*, AC-19(6):716–723, 12 1974.

[87] Hien D. Nguyen and Geoffrey J. McLachlan. Laplace mixture of linear experts. *Computational Statistics & Data Analysis*, 93:177 – 191, 2016.

[88] Stan Z. Li. *Markov Random Field Modeling in Image Analysis*. Springer-Verlag, Berlin, Heidelberg, 2001.

[89] Guillermo Terrén-Serrano, Adnan Bashir, Trilce Estrada, and Manel Martínez-Ramón. Girasol, a sky imaging and global solar irradiance dataset. *Data in Brief*, page 106914, 2021.